American Mineralogist, Volume 91, pages 635–657, 2006

Estimation of volume fractions of liquid and vapor phases in fluid inclusions, and definition of inclusion shapes

RONALD J. BAKKER[1,*] AND LARRYN W. DIAMOND[2]

[1]Department of Applied Geosciences and Geophysics, Mineralogy and Petrology Group, University of Leoben, Peter-Tunner-Strasse 5, A-8700 Leoben, Austria

[2]Institute of Geological Sciences, University of Bern, Baltzerstrasse 1-3, CH-3012 Bern, Switzerland

ABSTRACT

The molar volume (V_m) and chemical composition (x) of saline aqueous inclusions and gas inclusions in minerals can be calculated satisfactorily from microthermometric and other analytical data. For complex gas-bearing aqueous inclusions, however, calculation of $V_m - x$ properties requires additional input of the volume-fractions of the inclusion phases (φ). Traditional estimation of φ in non-fluorescing inclusions involves measuring area-fractions of the phases projected in the microscope and then making rough corrections for the third dimension. The uncertainties in the results are unknown and therefore the accuracies of the calculated $V_m - x$ properties are also unknown.

To alleviate this problem we present a new, routine method to estimate φ using the petrographic microscope in conjunction with a spindle-stage. Inclusions in normal thick-sections are rotated stepwise and their projected areas and area-fractions are plotted against rotation angle. The resulting data arrays are systematically related to inclusion orientation, to inclusion shape, and to φ. The dependency on orientation is minimized when area fractions are measured at the position where the inclusions project their largest total areas. The shape dependency is accounted for using a new objective classification of inclusion projections, based on parameters from digital image processing. The method has been verified with synthetic fluid inclusions of known φ. For individual liquid + vapor inclusions with regular (not "negative-crystal") shapes, the new procedure yields φ with a relative accuracy of ±4%. This degree of accuracy permits $V_m - x$ properties of gas-bearing, aqueous fluid inclusions to be calculated with sufficient certainty for many geochemical applications. Even better accuracy (e.g., down to ±0.6%) can be obtained by combining results from several inclusions in the same homogeneously trapped petrographic assemblage.

Keywords: fluid inclusions, new technique, shape definition, spindle stage, fluid phase, volume fractions

INTRODUCTION

Analysis of the chemical composition and bulk molar volume (or density) of fluid inclusions in minerals has undergone major advances in recent years with the advent of new quantitative analytical techniques, with the growth of the experimental database on the pressure, temperature, molar volume, and compositional (P-T-V_m-x) properties of geological fluids, and with the development of theoretical methods to model these fluids (for recent reviews see Andersen et al. 2001; Samson et al. 2003). Despite these advances, the analysis of saline aqueous inclusions that contain appreciable amounts of volatile components (e.g., CO_2, CH_4, H_2S, and N_2), which are common in diagenetic, hydrothermal, metamorphic, and igneous rocks, remains problematic. This is because the available equations-of-state for elevated P-T conditions are unable to link accurately high-T microthermometric measurements (homogenization temperatures) with low-temperature observations. The calculation of bulk properties still relies on notoriously inaccurate optical estimates of the volume fractions of phases (e.g., liquid and vapor) within the inclusions. Uncertainty in the phase volume-fractions is usually the greatest single contributor to the overall uncertainty in bulk $V_m - x$ properties of this important class of fluid inclusions (Diamond 2003a). Moreover, for most fluid-inclusion shapes, the magnitude of the uncertainty in volume fractions is unknown.

In addition to their use in calculating bulk inclusion properties, the volume fractions of phases in fluid inclusions at room temperature are routinely estimated during fluid inclusion petrography to deduce whether assemblages of cogenetic inclusions were originally trapped from a one-phase or a multi-phase pore fluid (e.g., Diamond 2003b). Although the absolute values of the volume fractions are less important for this purpose, and although other checks on the uniformity of compositions and densities can be made via microthermometry, the uncertainties currently inherent in determining the relative differences between cogenetic inclusions may lead to erroneous interpretations.

For fluids that fluoresce in ultraviolet light, such as petroleum-bearing inclusions, Pironon et al. (1998) and Aplin et al. (1999) showed that phase volume-fractions can be determined with acceptable accuracy using scanning confocal fluorescent

* E-mail: bakker@unileoben.ac.at

microscopy in reflected-light mode. The method involves integrating depth-series of two-dimensional images of individual inclusions, each with a very small optical depth-of-field. However, for the huge class of inclusions that do not contain fluorescent hydrocarbon molecules, the problem of measuring volume fractions remains unsolved. Phase contrasts in reflected light are too weak for reliable scanning confocal microscopy, and so most workers attempt to estimate phase volume-fractions from the two-dimensional projection (i.e., from the phase *area*-fraction) that is obtained using a conventional petrographic microscope illuminated by transmitted white light. The conversion from area- to volume-fractions is commonly performed by comparing the microscope image with published reference diagrams that display example inclusions with various three-dimensional shapes (e.g., Shepherd et al. 1985). Often a clue to the thickness of the inclusions along the *z*-axis can be obtained by varying the depth of focus within the sample, but on the whole the method is highly subjective and the results are at best semi-quantitative. As the petrographic microscope is still the most convenient instrument for routine fluid inclusion studies, any progress in improving the accuracy of phase-volume estimates using this instrument, or at least in quantifying the uncertainties of these estimates, is highly desirable.

In view of the above situation, we re-evaluate in this study the use of the petrographic microscope to estimate volume fractions of liquid and vapor in two-phase inclusions at room temperature. Our aims are (1) to quantify the probable uncertainties and (2) to suggest measurement procedures that could minimize the uncertainties. We begin by defining the mathematical equations that relate phase volume-fractions to bulk composition and molar volume (density), and, using these equations, we demonstrate how errors in volume fractions propagate into bulk $V_m - x$ analyses. After reviewing previous work on estimating phase volume-fractions, we explore the variability of the functional relationship between area fractions and volume fractions by simulating fluid inclusions with well-defined geometrical shapes. The corresponding relationships that can result in real inclusions are then illustrated using measurements on synthetic inclusions with known bulk $V_m - x$ properties. Here we compare results obtained by rotating individual inclusions on a spindle-stage with results from assemblages of inclusions viewed in fixed orientations. The empirical relationships between area fractions and volumes fractions are found to be systematic and predictable, and this opens the way for a reliable analytical methodology. The generalization of the results requires a simple, objective classification of the shapes of fluid inclusions. We therefore propose a new classification based on parameters measurable from series of two-dimensional images of individual inclusions obtained at different angles of rotation under the microscope. Finally, we organize our findings into a set of recommendations for determining the uncertainties of phase volume-fraction measurements during routine petrographic analysis.

Use of phase volume-fractions in calculating fluid inclusion composition and molar volume

The Standard International (S.I.) symbol for volume fraction is used here, namely, one of the two lower-case Greek letters for *phi* or "f", indicating "fraction" (Diamond 2003c). Older fluid inclusion literature uses a variety of symbols and definitions, e.g., F for "degree of fill", meaning the extent to which the inclusion is filled by liquid (the "vapor" being approximated by a vacuum); F_α for "volume fraction" of the subscripted phase; or R_α for "volume ratio" of the subscripted phase.

The volume fraction (φ) of a phase α in a fluid inclusion is defined as:

$$\varphi_\alpha = \frac{\text{Volume of phase } \alpha}{\text{Volume of inclusion}} \quad \text{where } 0 \le \varphi_\alpha \le 1. \tag{1}$$

Accordingly, φ_α has the dimensions of volume/volume and therefore it is unitless. Because phases in multi-phase fluid inclusions increase or diminish in size as a function of temperature, it is necessary to specify the temperature at which a volume-fraction measurement is made. For example, $\varphi_{vap}(20\ °C) = 0.40$ indicates that a vapor bubble occupies 40 vol% of the inclusion at 20 °C. In general, optical estimates of φ_α become even more complicated if more than two phases are present in an inclusion. Therefore, fluid inclusions that contain more than two phases at room temperature are usually heated until only two phases become stable, and the estimate of φ_α is made at this temperature.

The phase volume-fraction may be used along with other data to calculate the bulk $V_m - x$ properties of inclusions consisting of liquid and vapor. From Equation 1 it follows that:

$$\varphi_{liq} = 1 - \varphi_{vap} \tag{2}$$

where φ_{liq} and φ_{vap} are the volume fractions of the liquid and vapor phases, respectively. Thus, the bulk molar volume, V_m (or bulk density, ρ) of the inclusion is given by:

$$\frac{1}{V_m} = \frac{\varphi_{vap}}{V_m^{vap}} + \frac{1-\varphi_{vap}}{V_m^{liq}} \tag{3a}$$

$$\rho = \varphi_{vap} \cdot \rho^{vap} + (1 - \varphi_{vap}) \cdot \rho^{liq} \tag{3b}$$

where V_m^{vap} and V_m^{liq} are the individual molar volumes of the vapor and liquid phases, respectively, and ρ^{vap} and ρ^{liq} are the individual densities of the vapor and liquid phases, respectively. Values for the molar volumes of the individual phases must be obtained from independent sources and these must be valid for the temperature and pressure at which φ_{vap} is measured.

With bulk V_m now available from Equation 3a, the amount-of-substance fraction (hereafter referred to as the "mole fraction") of the vapor in the bulk inclusion, x_{vap}, can be calculated from:

$$x_{vap} = \frac{\left(V_m - V_m^{liq}\right)}{\left(V_m^{vap} - V_m^{liq}\right)}. \tag{4}$$

Finally, the concentration of each component i in the inclusion can be obtained from a mass-balance equation:

$$x_i = x_{vap} x_i^{vap} + (1 - x_{vap})\, x_i^{liq} \tag{5}$$

where x_i^{vap} is the mole fraction of component i in the vapor and x_i^{liq} is the mole fraction of component i in the liquid. Values for these two parameters may be obtained from microthermometric, Raman spectroscopic, or other analytical methods. Equation 5

is solved repeatedly for each component, *i*. Examples of such calculations are given by Bakker and Diamond (2000) and Diamond (2003a). The program package of Bakker (2003) incorporates equations equivalent to Equations 3 to 5 above, and performs calculations based on input from microthermometry and Raman analysis.

The dependency of bulk properties on φ_{vap} can be illustrated by solving Equations 3 to 5 for a specific example. For a particularly simple, binary case, consider a CO_2-H_2O fluid inclusion in which a liquid carbonic phase (car), a carbonic vapor, and an aqueous liquid (aq) are stable at low temperatures (e.g., 15 °C). This example corresponds to one of the synthetic fluid inclusions that is analyzed in a following section. The carbonic phases homogenize to liquid at 18 °C. At this temperature the internal pressure in the inclusion is 5.47 MPa, and V_m^{car} = 55.44 cm^3/mol and V_m^{aq} = 18.39 cm^3/mol (all values from the EoS of Diamond and Akinfiev 2003). If the measured volume fraction of the carbonic liquid is 54%, then solution of Equations 3 to 5 yields x_{CO_2} = 30% and V_m = 28.87 cm^3/mol. This example demonstrates that knowledge of the total homogenization temperature is not required to determine the bulk $V_m - x$ properties if φ_{vap} can be measured.

As pointed out above, the uncertainties in φ estimates are generally unknown. If we assume for the present example that the uncertainty in φ_{vap} is ± 10% (relative to the measured φ_{vap} value), or even ± 20%, then Equations 3 to 5 can be solved again to obtain new values of x_{CO_2} and V_m. Figure 1 shows the results of such error-propagation calculations. An error of +20% in φ_{vap}, for instance, yields x_{CO_2} = 39% (cf. the true value of 30%) and V_m = 32.58 cm^3/mol (cf. the true value of 28.87 cm^3·mol^{-1}). Errors of these magnitudes could have significant consequences for the application of fluid inclusion analyses in geochemical modeling.

Figure 2 shows the absolute errors in x_{CO_2} and V_m as a function of φ_{vap}, based on the same input data for Equations 3 to 5. It is clear that the example inclusion discussed so far is not necessarily a worst case. The propagated errors in bulk properties increase as φ_{vap} increases, reaching unacceptable levels as φ_{vap} exceeds 70%. However, at low values of φ_{vap}, for instance 5%, even a relative uncertainty of ±20% is unlikely to have serious consequences for geochemical applications of the result.

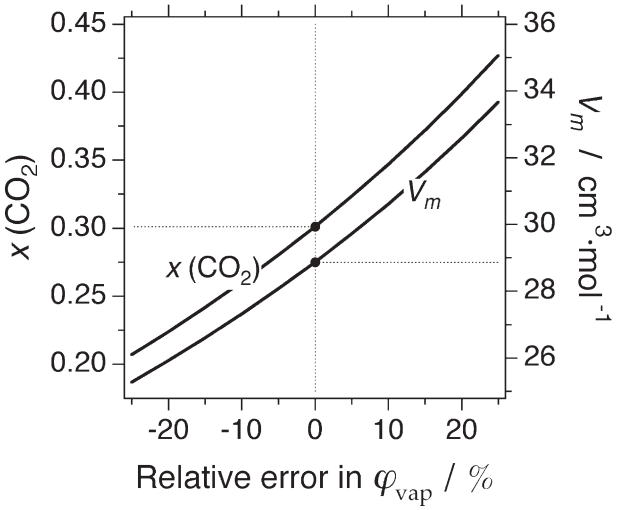

FIGURE 1. Propagation of errors in phase-volume fractions. The black dots show the true composition $x(CO_2)$ and bulk molar volume (V_m) of an example CO_2-H_2O inclusion that consists of liquid and vapor phases at room temperature. The curves show the effects on these calculated properties caused by errors in determining the volume fraction of the vapor phase (φ_{vap}). Relative errors on the order of ±20% are realistic for traditional methods of determining φ_{vap}.

Statement of the problem

Figure 3 illustrates the problem faced in determining phase volume-fractions from two-dimensional projections of fluid inclusions viewed through the petrographic microscope. In general, the microscope projection allows the area fraction (*a*) of a phase α to be measured, where

$$a_a = \frac{\text{Area of phase } \alpha}{\text{Area of inclusion}} \text{ where } 0 \le a_\alpha \le 1. \quad (6)$$

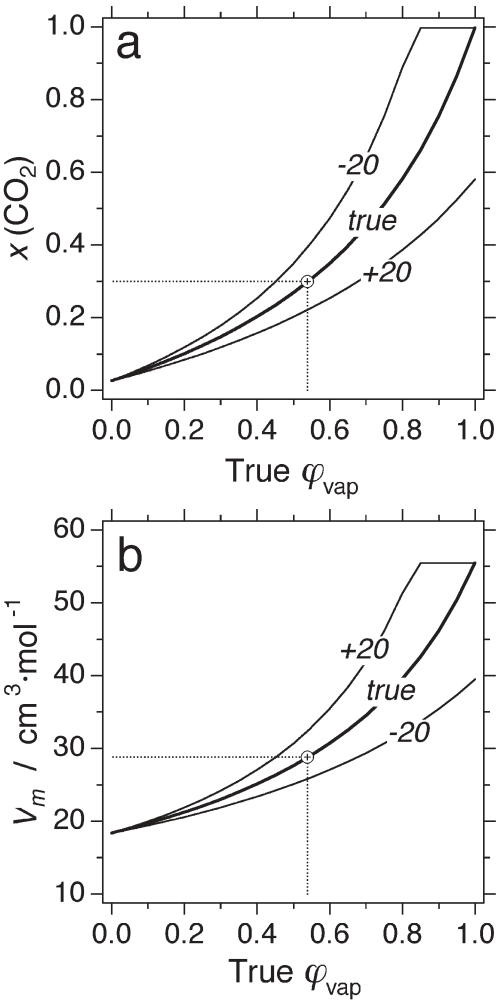

FIGURE 2. Propagation of errors in bulk fluid properties as a function of φ_{vap}. The curves marked "true" shows the true (**a**) composition and (**b**) bulk molar volume of fluid inclusions with the indicated φ_{vap} values (see text for data used in calculations). The dot represents the synthetic CO_2-H_2O inclusions used in this study. The curves marked –20 and +20 show the effects of propagating a relative error of ±20% in the determination of φ_{vap}.

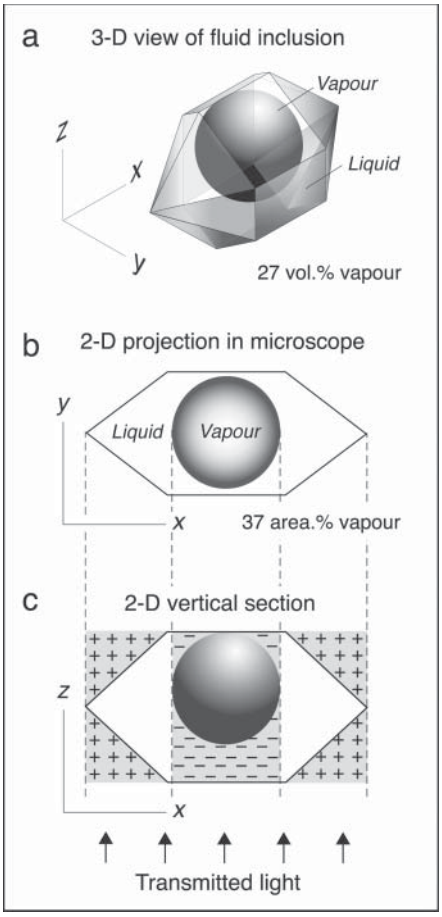

FIGURE 3. Summary of the problem faced in determining phase volume fractions from two-dimensional projections of fluid inclusions in the petrographic microscope. (**a**) Perspective view of hypothetical fluid inclusion with negative-crystal shape, in which the volume fraction of vapor is 27% (remaining 73 vol% is liquid). (**b**) When viewed parallel to *z* the area-fraction of vapor is 37%, which is a severe overestimate of the volume fraction. (**c**) Cross-section parallel to *xz* shows why the area fraction in (**b**) is a poor estimate of the true volume fraction of vapor; regions of liquid ("minus symbols") are overlooked in projection (**b**), and regions of host-crystal ("plus symbols") are implicitly attributed to liquid in projection (**b**). The divergence of the area fraction from the volume fraction is due to the relative weights of "plus" and "minus" areas when integrated over three dimensions.

Because a_α has the dimensions of area/area, it is unitless. Similarly to φ_α, a measurement of a_α is only meaningful if the temperature of the inclusion at the time of measurement is known.

Although area fractions can be measured readily using modern digital software, their relationship to volume fractions is not obvious. The difficulty arises from a combination of two opposing effects. On the one hand, the liquid lying above and below the bubble is invisible in two-dimensional projection, and hence it is not accounted for in the area fraction. The region of invisible liquid is marked with "minus" symbols in Figure 3c, indicating that its contribution to the volume fraction is generally underestimated. On the other hand, the inclination of the inclusion walls is not evident in projection, so the apparent amount of liquid is exaggerated in the area fraction. That is, some of what appears to be liquid is actually host crystal. The relevant area in Figure 3c is labeled with "plus" symbols to indicate that its contribution to the volume fraction is implicitly overestimated.

The situation in reality is much worse than suggested by Figure 3, because fluid inclusions display a huge range of shapes in the third (*z*) dimension, and because they usually have no axes of symmetry. Therefore, the relative weights of "plus" and "minus" regions, when integrated over three dimensions, can take on almost any value.

From the above considerations the area fraction appears to be a function of three variables: inclusion orientation, inclusion shape, and volume fraction. Thus,

$$a_{vap} = f(\text{orientation, shape, } \varphi_{vap}). \quad (7)$$

Our problem boils down to a search for a method that accounts for, or at least minimizes, the dependencies on orientation and shape, such that φ_{vap} can be estimated with useful accuracy.

Previous studies

Earlier workers have recognized the pitfalls in estimating phase volume-fractions in fluid inclusions from the two-dimensional projections of phase area-fractions. Roedder (1967, 1972), based on the work of Saylor (1965), pointed out that such projections may grossly underestimate bubble volumes owing to the curved upper surface of the inclusions acting as a strong negative lens. To illustrate this point, he showed how faceted inclusions may project different apparent diameters of the same bubble (Plate 11, Figs. 7–8 of Roedder 1972). Roedder (1967, Fig. 12.7) also calculated the difference between the projected area-fraction of a bubble and its true volume-fraction in the hypothetical cases of inclusions that are flat and circular or perfectly spherical. Depending on which case applies, the same area fraction corresponds to significantly different volume fractions. For a_{vap} = 34.1%, for example, the flat, circular inclusion has φ_{vap} = 34.1% whereas its spherical counterpart has φ_{vap} = 20% (see Fig. 12.7 in Roedder 1967 for other examples). This finding for the spherical model has often been adopted by subsequent workers as a rule that applies to all inclusion shapes. Projected area fractions are therefore widely assumed to *overestimate* the true volume fractions when the three-dimensional shape of the inclusion is unknown. Although Roedder (1984) warned that measurements of partly flattened or distorted bubbles yield only very crude and inconsistent estimates of phase volumes, and that visual estimates can be very inaccurate, no methods of quantifying the uncertainties have appeared in the literature so far.

The problem was highlighted again by Bodnar et al. (1985), who sketched a hypothetical fluid inclusion assemblage as it might be viewed through a petrographic microscope at room temperature. The sketch shows that many different values of a_{vap} may be observed if the inclusions have different orientations, even though the inclusions have similar shapes and exactly the same volume-fraction of vapor. That the phase-volume fractions are in fact uniform is demonstrable, in principle, if the assemblage shows a narrow range of homogenization temperatures. Nevertheless, the sketch shows a variation in a_{vap} of 31% to 100%,

implying that optical estimates of the volume fractions would have an enormous uncertainty if no information were obtainable on the thickness and shape of the inclusions in the *z*-axis. One could easily infer from this diagram that optical estimates of phase volume-fractions are too unreliable to be useful.

In recognition of the need for information on the shapes and thicknesses of inclusions in the *z*-axis, Anderson and Bodnar (1993) developed a spindle stage, which allows inclusion-bearing samples to be rotated about a horizontal axis and simultaneously viewed through the petrographic microscope at moderate magnification (e.g., using 40× or 36× long working-distance objective lenses). Although this stage has since been applied to characterize single inclusions for sophisticated analytical techniques, its application to determining phase volume-fractions in routine petrography has been limited. For the normal case, in which thick sections that contain many inclusions need to be examined prior to performing microthermometry, the optical clarity obtainable with the spindle stage usually restricts viewing to angles of rotation of less than 60°. This restriction is critical; it precludes the most obvious approach to solving the volume-fraction problem, namely of viewing individual inclusions at 90° intervals of rotation and then integrating to obtain volumes. A proven methodology of how to conduct volume-fraction measurements under routine, sub-optimal conditions is lacking.

Geometrical modeling of volume fractions

In a first step towards quantifying the dependency of area fraction on inclusion orientation and shape (according to Eq. 7), we explore the behavior of simple symmetrical shapes as models of fluid inclusions under the microscope. The aim of this exercise is to search for any promising systematic features or "rules of thumb" that may be exploited in a methodology for real asymmetrical inclusions.

The simplest case is when the inclusions are perfectly flat. Such inclusions pose no problems for determining phase volume fractions from two-dimensional projections, because as inclusion thickness (z) approaches zero,

$$\lim_{z\to 0}\left[a_{vap}\right] = \varphi_{vap}\,. \tag{8}$$

This relationship holds true even if the inclusions are not oriented perpendicular to the optical axis of the microscope. The accuracy of the φ_{vap} estimate therefore depends only on the certainty to which "flatness" can be recognized, and on the accuracy of the area measurements themselves.

Most inclusions have a finite thickness, and indeed gas-bearing aqueous inclusions, which are our main interest in this study, tend to have shapes that are more equant than those of gas-free aqueous inclusions (gas-bearing fluids wet mineral surfaces less readily). As demonstrated by Roedder (1967, 1972), spherical inclusions are also easy to deal with (see below), but they are rare in nature. Therefore, in addition to the spherical case we present numerical simulations of the relationships between a_{vap} and φ_{vap} for four hypothetical, geometrical shapes. The five models have been chosen to illustrate how different these relationships can be; they are not intended to cover all possible shapes of natural fluid inclusions.

Each model inclusion consists of a vapor bubble surrounded by liquid. Conceptually, the vapor is considered to expand progressively until it fills the inclusion completely. At each step in the expansion the orthogonally projected area fraction of the bubble (a_{vap}) is calculated and plotted against the corresponding volume fraction of the bubble (φ_{vap}). No account is taken of possible lens affects due to non-orthogonal refraction, as mentioned by Roedder (1972). In other words, the host crystal and the two fluid phases within the inclusion are all assumed to have the same index of refraction.

A spherical fluid inclusion has been modeled in Figure 4 so as to familiarize the reader with our choice of graphical display using a well-known example (cf. Roedder 1967). The vapor bubble is also assumed to be spherical, corresponding to minimal surface free-energy, therefore projections in any direction are equivalent; they all result in the same values of a_{vap}. The bubble is able to maintain its spherical form over all values of φ_{vap}, i.e., it is never deformed by the walls of the inclusion. In Figure 4 the curve labeled "***s***" lies entirely above the short-dashed 1:1 reference line, indicating that a_{vap} is always an overestimate of φ_{vap} (in a real inclusion the meniscus between vapor and liquid would probably become invisible at $\varphi_{vap} > 90\%$, owing to internal refraction of the transmitted light at the inclusion walls). The maximum relative divergence between a_{vap} and φ_{vap}, defined as $(a_{vap} - \varphi_{vap})/\varphi_{vap}$, occurs at a low value of φ_{vap} (< 10 vol%), whereas the maximum absolute divergence ($a_{vap} - \varphi_{vap} = +14.8\%$) occurs at 30 vol%.

A cylindrical inclusion terminated by hemispheres (Fig. 4) reveals a different correlation between a_{vap} and φ_{vap}. In the projection parallel to the long axis of this inclusion (***a*** in Fig. 4), both the inclusion and the bubble have circular outlines. For the inclusion dimensions chosen for this example, the bubble is able to expand spherically up to 22.2 vol% without being constrained by the walls of the inclusion (zone 1 in Fig. 4). At 22.2 vol% the

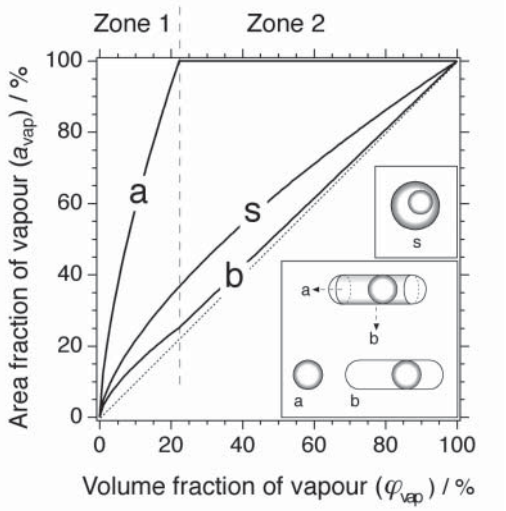

FIGURE 4. Volume fraction vs. area fraction diagram of the vapor bubble in spherical and cylindrical fluid inclusions. The cylinder has a relative length of 28 and a radius of 6. The ends of the cylinder are hemispheres with a radius of 6. The spherical inclusion projects equally in all directions (***s***), whereas the cylindrical inclusion appears spherical in the ***a*** projection and elongate in the ***b*** projection. See text for further details.

bubble makes contact with the inclusion walls along its entire projected perimeter, and so the projection parallel to ***a*** results in a_{vap} equal to 100%. No further changes in a_{vap} are visible in this projection as j_{vap} increases above 22.2 vol% (zone 2, Fig. 4). Figure 4 thus shows that all values of a_{vap} on curve ***a*** are extreme overestimates of the corresponding j_{vap}. In any projection perpendicular to ***a***, such as ***b*** in Figure 4, the elongate shape of the inclusion is revealed, and the bubble may be observed to expand steadily along the length of the cylinder at φ_{vap} greater than 22.2%. Curve ***b*** shows that the values of a_{vap} correspond closely to those of φ_{vap}, although they remain slight overestimates. As found for the spherical inclusion, the relative divergence of a_{vap} from φ_{vap} reaches its maximum value at low φ_{vap} (in zone 1), though this value is much lower than for spherical inclusions. For the ratios of inclusion dimensions in this example, the absolute divergence reaches a maximum of +4.8% at 11 vol%.

Figures 5, 6, and 7 illustrate the calculated $a_{vap} - \varphi_{vap}$ relationships for model inclusions with the shape of a tetragonal prism, a truncated cone, and a hexagonal prism (the latter terminated either by hexagonal pyramids or by pinacoids). These diagrams are to be interpreted in the same way as Figure 4. In projections parallel to the long axis (***a***), where the inclusions appear in their smallest dimensions, a_{vap} increases rapidly with increasing φ_{vap} so long as the bubble is free to expand, unconstrained by the walls of the inclusions (zone 1). Once the bubble has expanded to the point where it can increase in size only by deviating from a spherical cross-section parallel to ***a*** (zone 2), the projected a_{vap} along ***a*** remains constant, and strongly overestimates φ_{vap}. In orientations where the maximum total area of the inclusions is projected through the microscope (curve ***b*** in Figure 6 and curves ***c*** in Figures 5 and 7), the values of a_{vap} initially lie close to φ_{vap}. However, as the volume of the bubble increases beyond about 60%, a_{vap} becomes increasingly *smaller* than φ_{vap}. In Figure 7, the elongate form of a hexagonal prism terminated by hexagonal pyramids (a shape approaching the common habit of a quartz crystal) is shown by the continuous curves ***b*** and ***c***. If the hexagonal prism is terminated by pinacoids (a common habit of tourmaline, for example), then the correlations between a_{vap} and φ_{vap} (long-dashed curves in Fig. 7) more closely approach those of the tetragonal prism in Figure 5 (a common shape of inclusions in fluorite and halite, for example).

The segments of curves in Figures 5, 6, and 7 with a_{vap} values *smaller* than φ_{vap} are explained by the relative position of the bubble within the inclusion: the bubble always occupies the

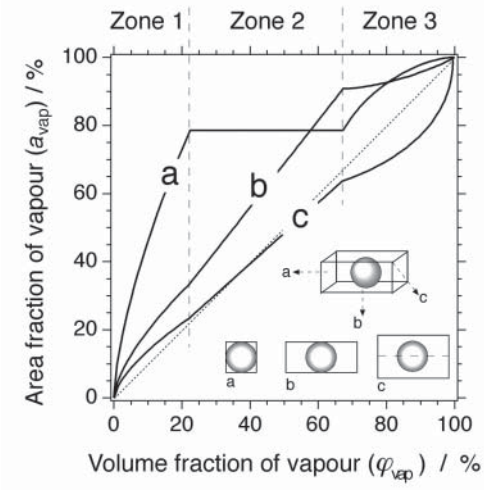

FIGURE 5. Volume fraction vs. area fraction diagram of the vapor bubble in an inclusion with the shape of a tetragonal prism (elongate block shape with six faces and 90° interfacial angles). The relative dimensions of the prism are 28 × 12 × 12. Projections in the directions ***a***, ***b***, and ***c*** have various sizes. Projection ***c*** is oriented 45° to ***b*** and perpendicular to ***a***.

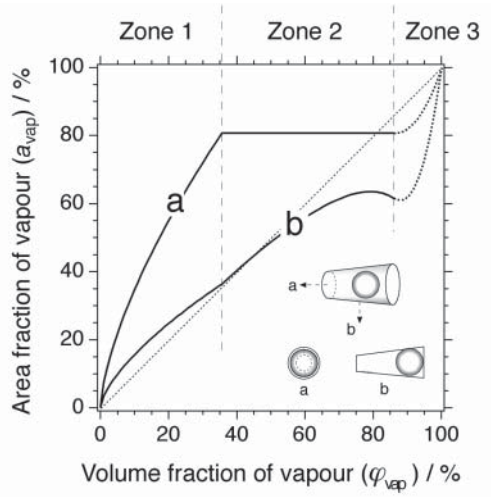

FIGURE 6. Volume fraction vs. area fraction diagram of the vapor bubble in an inclusion with the shape of a truncated cone. The relative length of the cone is 28, the top radius is 3, and bottom radius is 6. The inclusion appears spherical in the ***a*** projection and elongate in the ***b*** projection.

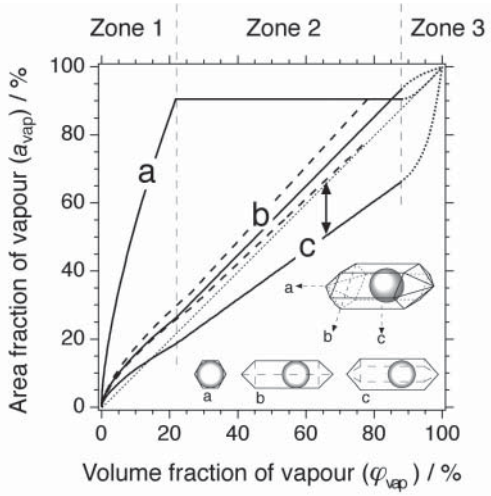

FIGURE 7. Volume fraction vs. area fraction diagram of the vapor bubble in an inclusion with the shape of a "negative" quartz crystal (hexagonal prism with hexagonal pyramids). Each face of the hexagonal prism has a relative size of $28 \times 4\sqrt{3}$. The hexagonal pyramids that terminate the prism have a relative length of 6. Projections in the directions ***a***, ***b***, and ***c*** have various sizes. The ***c*** projection lies perpendicular to a prism face, and the ***b*** projection bisects the 120° angle between prism faces. Long-dashed curves show the corresponding relationships for a hexagonal prism terminated by pinacoids. See the text for further details.

largest three-dimensional region within the inclusion, where it may approach a spherical shape and thereby minimize its surface free-energy. The liquid phase occupies narrower and flatter parts of the inclusion, thus exaggerating its area fraction and causing a relatively large underestimation of φ_{vap} in two-dimensional projections.

Although the results for the non-spherical models plotted in Figures 5 to 7 are strictly valid only for the chosen inclusion dimensions, several very useful conclusions can be drawn. First, the figures clearly invalidate the common assumption that a_{vap} always overestimates φ_{vap}. The value of a_{vap} may be greater than or less than φ_{vap}, depending on the shape and orientation of the inclusion. Second, the divergence between a_{vap} and φ_{vap} appears to be minimized, in general, when the inclusions are oriented such that their largest areas are projected through the microscope. This is the systematic "rule of thumb" that was sought at the outset of this section and which will be exploited in following sections where a_{vap} measurements are made of real inclusions.

Geometrical modeling of area fractions

Among the experimental results presented below are measurements of projected inclusion areas (A_{tot}) as a function of sample rotation angle (θ). To aid interpretation of the ensuing A_{tot}-θ graphs, the theoretical behavior of several geometrical shapes has been calculated and plotted in Figure 8. Again, no account has been taken of non-orthogonal optical effects in the projections.

The most extreme changes in projected area upon rotation are displayed by flat inclusions (solid parabolas in Figs. 8a and 8b). Spherical inclusions, in contrast, show no changes upon rotation (horizontal lines in Figs. 8a and 8b). A cylindrical inclusion terminated by hemispheres (Fig. 8a) with an aspect ratio (diameter/length) of 0.3 represents the inclusion modeled in Figure 4. Its maximum reduction in area is caused by rotation about the *y*-axis (dashed parabola labeled *y*), whereas A_{tot} remains constant upon rotation about the *x* or *z*-axes (horizontal line labeled *x*,*y*; coincident with the sphere). Consequently, a randomly oriented population of cylindrical inclusions with a fixed rotation axis (as in a thick section mounted on a spindle stage) will describe a family of curves that lie between these limiting cases (shaded area in Fig. 8a). The maximum changes in A_{tot} for similar cylinders with aspect ratios of 0.5 and 0.8 are plotted in Figure 8a for comparison (dashed curves).

Figure 8b shows the changes in projected area of a tetragonal prism terminated by pinacoids, as modeled in Figure 5 (the curves for flat and spherical inclusions are also included for reference). The reduction in area upon rotation about the *y*-axis (dashed curves in Fig. 8b) exhibits the same parabolic behavior as perfectly flat inclusions, whereas A_{tot} remains constant if rotation is about the *z*-axis. Again, rotation of a randomly orientated population of inclusions with this fixed shape and aspect ratio will describe a family of curves between the bounding cases. This example illustrates that a strong reduction in area upon rotation cannot be used alone as a criterion for identifying flat inclusions. Essentially flat inclusions are best recognized by the combined criteria of parabolic reduction in A_{tot} according to $\cos(\theta)$, plus nearly constant a_{vap} values. The projected areas of prisms upon rotation may follow the curve for flat inclusions, but after a certain θ–interval a minimum in the A_{tot}-θ curve is reached, and further rotation causes the area to increase again. For example, the dashed curves in Figure 8b show how a tetragonal prism oriented with one side up can be rotated by 45° before the parabolic trend of decreasing area is reversed (dashed curves in Fig. 8b).

The geometrical models in Figures 4, 5, 6, and 7 display the divergence of a_{vap} from φ_{vap} along projections parallel to the principal dimensions of the inclusions, without any rotation. Figures 8c and 8d illustrate for the same models the variation of a_{vap} with respect to the angle α between the longest dimensions of the inclusions and a rotation axis. Calculations have been made for inclusions with φ_{vap} of 25%, 50%, and 75%. The inclusions are oriented such that their largest areas are projected, i.e., parallel to projection ***b*** in Figure 4 and projection ***c*** in Figures 5 and 7. The cylindrical inclusion undergoes a monotonic increase in a_{vap} with increasing α (solid curves in Fig. 8c), whereas the tetragonal prism passes through minima at 18° for $\varphi_{vap} = 25\%$, at 34° for $\varphi_{vap} = 50\%$, and at 40° for $\varphi_{vap} = 75\%$ (dashed curves in Fig. 8c). At high φ_{vap} the tetragonal prism projects a_{vap} values that underestimate φ_{vap} over a large range of α, whereas the cylinder always projects overestimated values. The dashed curves in Figure 8d show that the degree of overestimation of φ_{vap} is even greater in the case of a hexagonal prism terminated by pyramids (same shape as modeled in Fig. 7). A hexagonal prism terminated by pinacoids displays a behavior between that of a cylinder and a tetragonal prism (solid curves in Fig. 8d).

Experimental method

The above modeling suggests that, if symmetrical fluid inclusions are oriented such that their largest areas are projected in the microscope, the relationship between a_{vap} and φ_{vap} is simplified. To investigate to what extent this rule is valid for real asymmetrical inclusions, test samples are required with known φ_{vap} values. Fluid inclusions were synthesized for this purpose according to the method of Bodnar and Sterner (1987) by healing fractures (induced by thermal shock) in rods of natural, inclusion-free, Brazilian quartz. In a first synthesis, pure H_2O was held in contact with the quartz for one week at 580 °C and 79 MPa, yielding inclusions with critical molar volume (56.0 $cm^3 \cdot mol^{-1}$ or 0.322 $g \cdot cm^{-1}$). In a second synthesis, pure H_2O inclusions were made in nine days at 544 °C and 445.5 MPa, yielding inclusions with a molar volume of 21.8 cm^3/mol (0.826 g/cm). In a third synthesis, pure H_2O and silver oxalate were used to generate a homogeneous H_2O-CO_2 fluid containing 30 mol% CO_2. This fluid was maintained in contact with the quartz for four weeks at 600 °C and 500 MPa, producing inclusions with a molar volume of 28.87 cm^3/mol (0.894 g/cm).

After the experiments, the quartz rods were cut into disks and polished on both sides to allow microscopic observation and microthermometry. The inclusions from the shorter experiments (pure H_2O) generally have irregular, flat shapes, but some regular, equant inclusions are also present. At room temperature (20 °C) all the inclusions in the first synthesis contain a vapor bubble that is calculated to be 67.8 vol%, the remainder being liquid water (the equation of state of Wagner and Pruss 2002 was used for the calculations). The inclusions homogenize between 373 and 375 °C via the critical phase transition. In the second sample of H_2O inclusions the vapor bubble is calculated to fill 17.4 ± 0.07 vol% of the inclusions at room temperature, and homogenization occurs via a bubble-point transition between 230.4 and 231.4 °C. The H_2O-CO_2 inclusions from the third experiment generally have more regular shapes and are equant, some of them approaching the shape of a "negative" quartz crystal. The CO_2 phases homogenize to liquid CO_2 between 16.2 and 18.0 °C, such that at room temperature (20 °C) they contain one bubble of liquid CO_2 (calculated to be 53.8 ± 0.25 vol%; see example above using Eqs. 3 to 5 and the listed input data), rimmed by aqueous liquid. These two phases in turn homogenize to a liquid phase between 280.9 and 287.3 °C. For simplicity, the room-temperature phase assemblage of these inclusions (dense aqueous liquid + less-dense CO_2 liquid) is hereafter referred to simply as liquid + "vapor".

Following microthermometry the quartz disks were glued to a metal stub that was fixed magnetically to a spindle stage (Anderson and Bodnar 1993), and im-

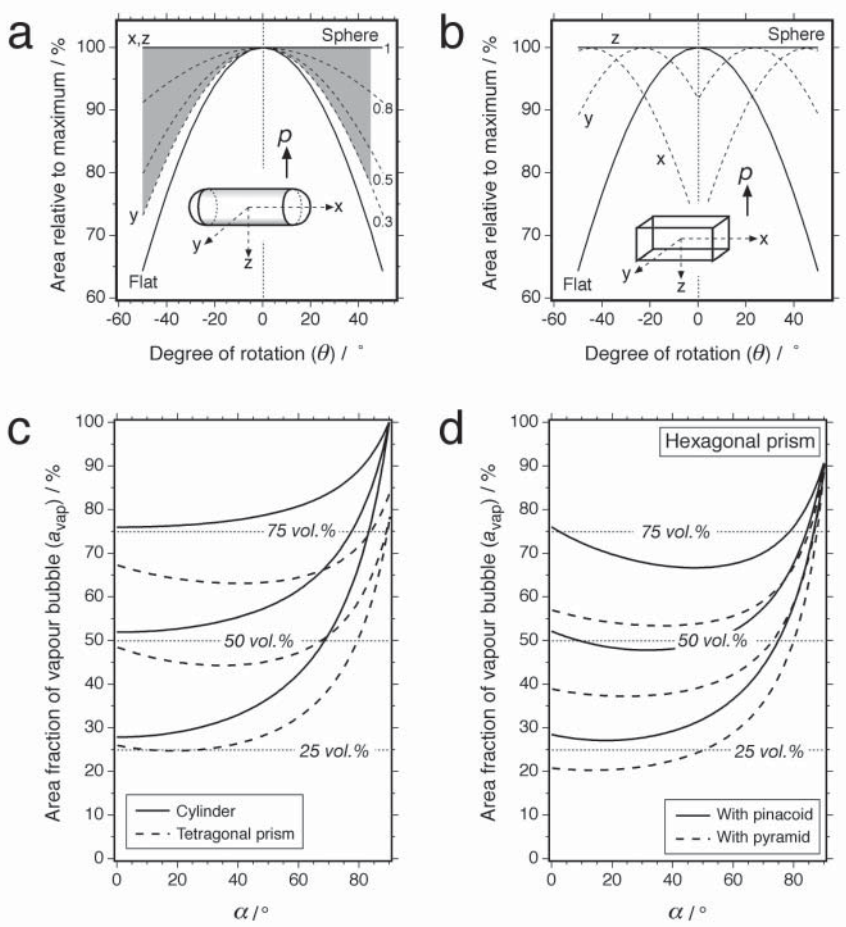

FIGURE 8. Calculated projections of the geometrical inclusions in Figures 4 to 7. The arrow marked p shows the projection direction. (**a**) Projected total areas of flat, spherical, and cylindrical inclusions vs. angle of rotation θ (e.g., on a spindle stage) along axes *x*, *y*, and *z*. (**b**) Projected total areas of a tetragonal prism vs. angle of rotation, θ, along axes *x*, *y*, and *z*. (**c**) Projected area fractions of the vapor bubble in cylindrical (solid curves) and tetragonal-prism (dashed) inclusions, vs. the angle α between the longest dimension of the inclusion and a spindle-stage rotation axis. (**d**) Same as (**c**) but calculated for inclusions shaped like "negative" quartz crystals: hexagonal prisms terminated by pinacoids (solid curves) or by hexagonal pyramids (dashed).

mersed in a cell containing oil with a refractive index similar to those of quartz. The assembly was mounted on a microscope with a 40× long-working-distance objective lens fitted with an adjustable cover-slip correction cap. The face of the objective lens was situated in air, above the upper level of immersion oil in the sample cell. The samples were viewed with a sub-stage condenser lens inserted into the light path. In this configuration the convergent transmitted light entered the immersion oil from below the sample. The light then traversed the inclusion-bearing quartz sample, passed through the overlying oil, and exited into air before entering the objective lens. The spindle stage was thus used in the exactly the same way as described by Anderson and Bodnar (1993).

Each inclusion selected for area measurement was aligned approximately along the rotation axis of the spindle stage. The sample was then rotated in intervals of 5° and the inclusion was photographed digitally in each position. The value of a_{vap} in each microphotograph was measured by tracing digitally around the *outside* edges of the shadows that define the perimeters of the bubble and the inclusion. Tests showed that tracing around the outside edges yielded the greatest reproducibility in a_{vap}, especially when different workers measured the same inclusion. Presumably the outermost outline best represents the true projection of the three-dimensional inclusion. Areas were integrated with the NIH image software package (version 1.63) or its successor, ImageJ (http://rsb.info.nih.gov/).

Owing to optical effects related to depth-of-focus and refraction, the clarity of the outlines of the inclusions and their bubbles varied with orientation of the disk. To help account for this inherent uncertainty, the a_{vap} measurements were repeated three times for each microphotograph. The first trace was performed in a clockwise direction, the second anticlockwise, and then the photograph was enlarged by 200% and traced a third time. In addition, the total area and the perimeter of each inclusion were measured from each microphotograph.

Several target inclusions had such irregular shapes that their entire outlines could not be brought into focus at any one vertical position of the microscope stage. Photographs were unsuitable in these cases, therefore the inclusion and bubble outlines were traced by hand using a projection tube mounted above the trinocular head of the microscope. The scale drawings were then digitized and thereafter treated in the same way as the photographs.

RESULTS

Within each of the three synthetic fluid inclusion samples, several inclusions representing a variety of shapes were selected for analysis. The aim was to search for reproducible patterns in the relationships of projection angle, fluid inclusion area, and a_{vap}, with respect to φ_{vap}. The results for three representative inclusions from each sample are presented in the following. Additional results are available on the authors' websites (http://fluids.unileoben.ac.at/ and www.geo.unibe.ch/diamond). As a complement to the analyses of individual fluid inclusions, measurements of a_{vap} were also made on assemblages of inclusions in each sample, with the quartz disks in fixed orientations. All measurements, on both individual inclusions and assemblages, were made at 20 °C.

Measurements of individual synthetic H_2O inclusions with 67.8 vol% vapor

Figure 9 summarizes measurements on a slightly conical inclusion. Figures 9a–c show the view through the microscope at three angles of rotation (θ), with the axis of the spindle stage oriented parallel to the short dimension of the printed page. Thus, the long axis of the inclusion lies at about 70° from the axis of the spindle-stage (this is the angle α plotted in Figs. 8c and 8d). A θ value of zero is assigned to the horizontal position of the fluid

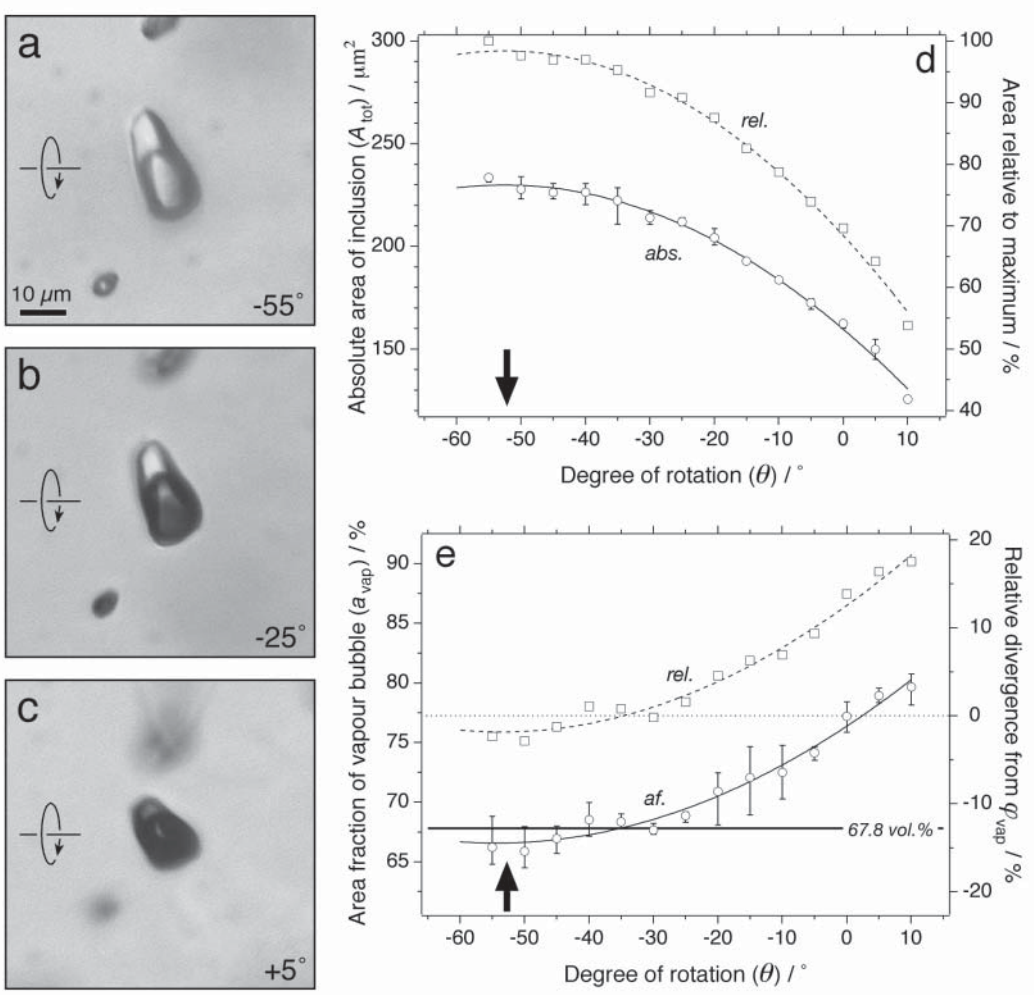

FIGURE 9. Projected areas of a slightly conical, synthetic H_2O inclusion in quartz, containing 67.8 vol% vapor. (**a**, **b**, **c**) Microscope projections of the inclusion at three different angles of rotation (θ) in the spindle stage (numbers indicate angles). The axis of rotation is schematically illustrated. (**d**) Absolute projected area of the inclusion (left-hand ordinate scale) and area relative to the maximum area (right-hand scale), both vs. θ. The arrow marks the angle at which the maximum area of the inclusion is projected. (**e**) Area fractions of the vapor bubble as a function of θ. The horizontal reference line indicates the volume fraction of vapor (67.8%). The solid curve shows the absolute values of the area fraction (with respect to the left-hand ordinate scale). The dashed curve (with respect to the right-hand scale) shows the relative divergence of the area fraction from the known volume fraction $[(a_{vap} - \varphi_{vap})/\varphi_{vap}]$. The mean absolute divergence at the angle of the maximum projected area (a_{vap}* $- \varphi_{vap}$) is –1.5 vol% (arrow).

inclusion sample in the spindle stage, a positive sign indicates rotation in a clockwise direction, and a minus sign denotes an anticlockwise rotation; for example, Figure 9a shows the inclusion after 55° anticlockwise rotation, whereas Figure 9c shows the same inclusion after 5° clockwise rotation.

Figures 9a–c are not perfectly sharp. Certain segments of the outlines in Figures 9a and 9c are fuzzy, and an optical artifact (a Becke line) is visible as a bright rim along the left side of the inclusion in Figure 9a and as a dark shadow in Figure 9b. The quality of the images is evidently less than optimal for area measurements, but it is typical of all the inclusions studied here, and it is typical of most fluid inclusions in natural samples.

Figure 9d displays the projected area of the inclusion, A_{tot}, as a function of rotation angle. The ranges of the triplicate measurements (in absolute values of μm²; see scale on left-hand ordinate) are indicated by the error bars, and the mean of each triplicate is plotted as a circle. Because the quality of the images varies from one rotation position to another, the length of the error bars also varies in a unpredictable way. The entire set of data was regressed to a best-fit polynomial function to smooth the trends (solid curve, labeled "*abs.*"). It is obvious that the inclusion appears smallest near 10° and that the projected area increases as the inclusion is rotated to –55°. The maximum projected area according to the fitted curve lies around –52° (marked by an arrow in Fig. 9d).

The mean values of the absolute areas plotted in Figure 9d have been recalculated relative to the maximum datum found at –55°. The square symbols in Figure 9d show these recalculated values (see scale on right-hand ordinate), and the dashed curve labeled "rel." represents a best-fit polynomial function to the mean of each set of triplicate data. Thus, the largest mean area plots at 100% and the smallest area (found at 10° rotation) plots

at 54%. By comparison with Figure 8a, the form of the dashed A_{tot}-θ curve confirms that the inclusion is neither spherical (the line would be horizontal) nor perfectly flat (the curve would drop to around 71% at 45° from the maximum, whereas the curve in Fig. 9d drops to only 76%). Also, the dashed curve undergoes no inflections upon 45° of rotation, as would be the case if the inclusion had a tetragonal shape (cf. Fig. 8b).

Figure 9e displays a_{vap} as a function of rotation angle. The ranges of triplicate measurements are shown by the error bars and the mean values are indicated by circles, all with respect to the scale on the left-hand ordinate. The solid curve labeled "af." shows the best-fit polynomial function. To illustrate the relationship between a_{vap} and φ_{vap}, the value of φ_{vap} (67.8%) is marked by the thick horizontal line, with respect to the same ordinate scale as a_{vap}. It is obvious that a_{vap} grossly overestimates φ_{vap} at θ values near 10°, but after more than –35° rotation the mean values of a_{vap} drop slightly below φ_{vap}. This behavior is reminiscent of the symmetrical cone plotted in Figure 6. For an inclusion with φ_{vap} equal to 67.8%, a_{vap} along the ***a*** projection (compare inset diagram ***a*** in Fig. 6 with Fig. 9c) lies well above the true φ_{vap} value, whereas along the ***b*** projection the value of a_{vap} underestimates φ_{vap} (compare inset diagram ***b*** in Fig. 6 with Fig. 9a). However, it is obvious that the inclusion in Figures 9a,b,c is not a perfectly symmetrical cone and that the rotation axis of the photographed inclusion is probably oriented between the ***a*** and ***b*** axes in Figure 6. The similarities between Figures 6 and 9 are therefore only qualitative.

The object of plotting the analyses in Figure 9 is to reveal any systematic relationships between a_{vap} and φ_{vap}. Although the a_{vap}-θ curve in Figure 9e intersects the φ_{vap} reference line at approximately –35°, this fortunate angle cannot be deduced solely from the curves in Figure 9d; they show no special features at this angle. The only features of the curves that can be identified objectively are the maxima. Figure 9e shows that, at the angle of these maxima (marked by the arrow at –52°), a_{vap} is still equal to φ_{vap} within the reproducibility of the measurements.

The mean relative divergence of a_{vap} from φ_{vap} is indicated in Figure 9e by the square symbols and by the dashed curve (both with respect to the scale on the right-hand ordinate). Thus, the mean a_{vap} at 10° rotation is seen to overestimate φ_{vap} by 18%, whereas at –52° rotation (arrow in Figure 9e), the mean a_{vap} underestimates φ_{vap} by only 2%.

Several of the regular-shaped inclusions analyzed below show a close match between a_{vap} and φ_{vap} at the rotation angle at which the maximum area of the inclusions is projected. For further reference this special angle is denoted by the symbol θ* and the corresponding value of a_{vap} by the symbol a_{vap}*. The position of θ* in each of the following A_{tot}-θ and a_{vap}-θ diagrams is marked with heavy arrows.

Figure 10 illustrates an elongate inclusion with a roughly cylindrical shape. The long axis of the inclusion is oriented at about 40° to the axis of the spindle stage. The cylindrical nature of the inclusion is demonstrated by its similar appearance over 60° of rotation (compare Fig. 10a at –30° with Fig. 10b at 0° and Fig. 10c at 30°). The A_{tot}-θ curves in Figure 10d show maxima at –27° rotation. The dashed curve in Figure 10d, showing the area of the inclusion relative to its maximum area, is somewhat similar to the dashed curve in Figure 8a, which represents a symmetrical cylinder with aspect ratio of 0.4; both curves fall to about 80% upon 45° rotation from θ*. As shown in Figure 10e, the measurements of a_{vap} for this inclusion are not very reproducible (e.g., at –25° the range is from 64% to 71%). However, the regressed polynomial function (solid curve) provides a smooth trend. At +35°, where the inclusion displays its smallest area (cf. Fig. 10d), the value of a_{vap} strongly overestimates φ_{vap} (by 14% on the relative scale). This is not unlike the behavior of the symmetrical cylinder shown in Figure 4 (curve ***a***) and Figure 8c (dashed curve 50 vol%), even though the axes of rotation are not quite comparable. Between 5° and –35° the a_{vap}-θ curve in Figure 10e flattens out and lies very close to φ_{vap}, again similar to the behavior of a symmetrical cylinder (cf. curve ***b*** in Fig. 4). At θ* (–27°), a_{vap}* matches φ_{vap} to well within the uncertainty of the measurements.

Figure 11 shows measurements for an approximately equant inclusion with a distinct "negative-crystal" shape (most obvious in Figure 11a). The longest axis of the inclusion is oriented parallel to the axis of rotation of the spindle-stage. As in Figures 9 and 10, a_{vap} overestimates φ_{vap} at the rotation angle corresponding to the smallest observed projection of the inclusion (–35°). This is expected from qualitative comparison with the geometrical model in Figure 7 (projection ***b***), even though the minimum area of the inclusion was not found in the analyses (the A_{tot}-θ curves in Fig. 11d do not exhibit minima). Near the maxima in the A_{tot}-θ curves (θ* = 35°), the values of a_{vap} level off at about 60%, strongly underestimating φ_{vap} (–12% divergence on the relative scale of Fig. 11e). Thus, in contrast to the regular-shaped inclusions in Figures 9 and 10, a_{vap}* is a very poor estimate of φ_{vap}.

A large, highly irregular, ladle-shaped inclusion is displayed in Figure 12. The complexity of the shape in three dimensions made it impossible to focus the entire inclusion in the microscope at one time (cf. Figs. 12a, 12c). To provide more accurate outlines, drawings were made of the inclusion (see Experimental Method) by varying the focus level of the microscope (e.g., Fig. 12a' and 12c'). The open symbols in Figures 12d and e show triplicate measurements made from the set of partly focused photographs. The solid symbols in Figure 12e show a_{vap} measurements made on the drawings (one per 5° rotation interval). Between –55° and +10° rotation the results from the drawings are lower than those from the photographs, but the trend reverses at higher θ. The a_{vap} values from the drawings are probably more accurate. Their reproducibility compared to the photographic method cannot be assessed, because only one drawing was made per rotation interval. At θ* (–27°), as over much of the measured θ range, a_{vap}* underestimates φ_{vap} by 22% on the relative scale (dashed curve labeled "m" in Figure 12e). Evidently, the amount of liquid in the handle of the ladle is strongly exaggerated in the projections, similarly to the regions marked with plus symbols in Figure 3. The open arrows in the photographs in Figures 12b and c point to a rim of liquid between the vapor bubble and the inclusion wall. The drawings (Fig.12c'), however, show that this "rim" is an optical artifact (caused by non-orthogonal refraction of the transmitted light), and that the bubble actually extends to the inclusion wall.

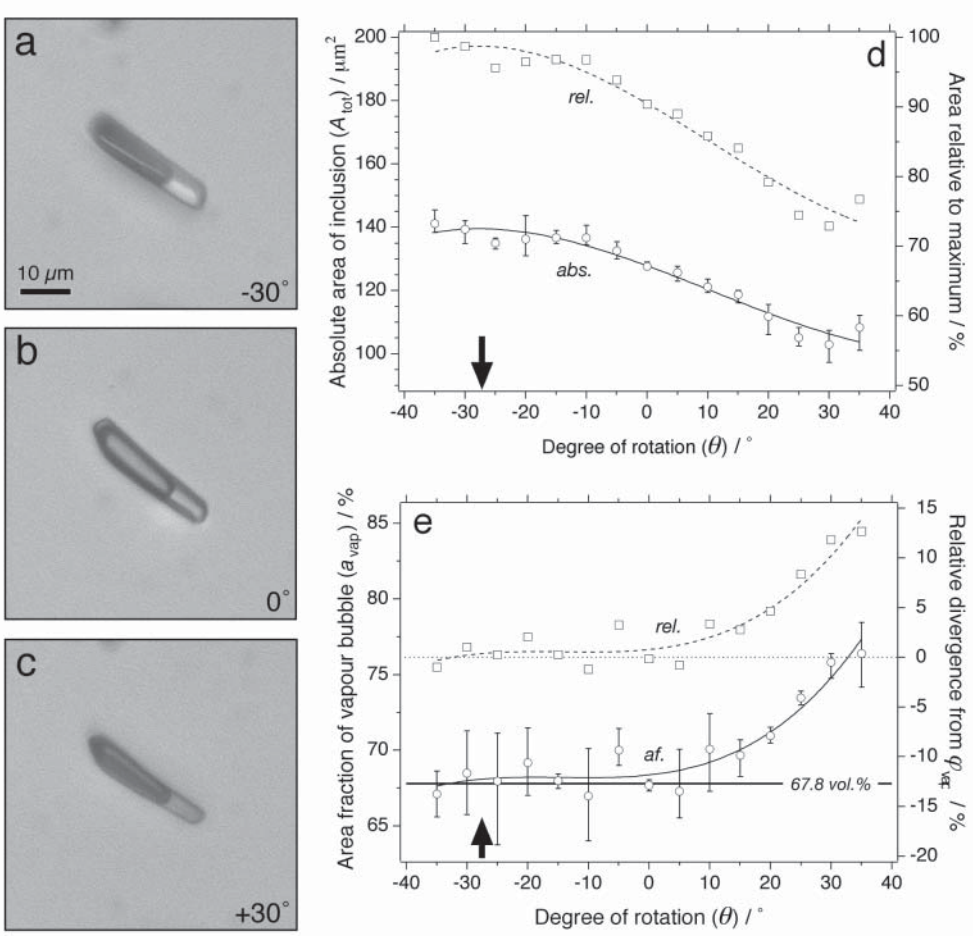

FIGURE 10. Projected areas of an elongate synthetic H_2O inclusion in quartz, containing 67.8 vol% vapor. See caption to Figure 9 for description. The mean absolute divergence at the angle of the maximum projected area (a_{vap}* – φ_{vap}) is 0.4 vol% (arrow in **e**).

Measurements of individual synthetic H_2O inclusions with 17.4 vol% vapor

The results for a small equant inclusion are shown in Figure 13. The longest dimension of the inclusion is oriented roughly perpendicular to the axis of the spindle stage. The photographs at high angles of rotation (Fig. 13a and 13c) are of poor definition, which hinders accurate measurement of A_{tot} and a_{vap}. Figure 13a shows strong double-refraction (a blurred duplicate image of the inclusion appears to the left of the central image), which could not be eliminated entirely using a sub-stage polarizer. The difficulty in defining the inclusion outlines is reflected in the large error bars of the a_{vap} measurements at high and low values of θ (Fig. 13e). Also, the A_{tot} values for –20° and –25° (marked by black symbols in Figs. 13d and 13e) diverge strongly from the general trend, again owing to optical problems, and so these data were omitted from the set fitted by polynomial curves. The dashed A_{tot}-θ curve in Figure 13d falls to 78% of its maximum upon 45° of rotation, proving that the inclusion is neither flat nor spherical (cf. Fig. 8a). Indeed, the inclusion is difficult to compare with any of the geometrical shapes shown in Figures 4 to 7. Probably a cylinder is closest, as all the a_{vap} values in Figure 13e are greater than φ_{vap}, similar to projections ***a*** and ***b*** in Figure 4. The maxima of the A_{tot}-θ curves lie at –15° and the mean a_{vap}* overestimates φ_{vap} by 8% on the relative scale. However, φ_{vap} lies within 1.33σ of the 3 triplicate a_{vap} data near θ*, where σ is the standard deviation (see also Table 1).

Figure 14 shows a pinched cylindrical inclusion with its long axis oriented at a small angle to the spindle stage. The inclusion is slightly bent, judging from the difference in orientation of its longest axis between Figures 14a and b. The dashed A_{tot}-θ curve in Figure 14d falls to 78% of its maximum upon 45° of rotation (at θ = 55° or –35°), which is similar to the behavior of a cylinder with an aspect ratio of 0.3, as shown in Figure 8a. The synthetic inclusion is not quite symmetrical; it appears somewhat flatter in Figure 14a that in Figures 14b or 14c. Nevertheless, like the ***a*** projection of the symmetrical cylinder modeled in Figure 4, a_{vap} is greater than φ_{vap} at angles of rotation where the projected inclusion areas are small. At angles where the projections are largest, a_{vap} is either very close to φ_{vap} (similar to projection ***b*** in Figure 4) or less than φ_{vap}. At θ* (10°), a_{vap}* underestimates φ_{vap} by 4%

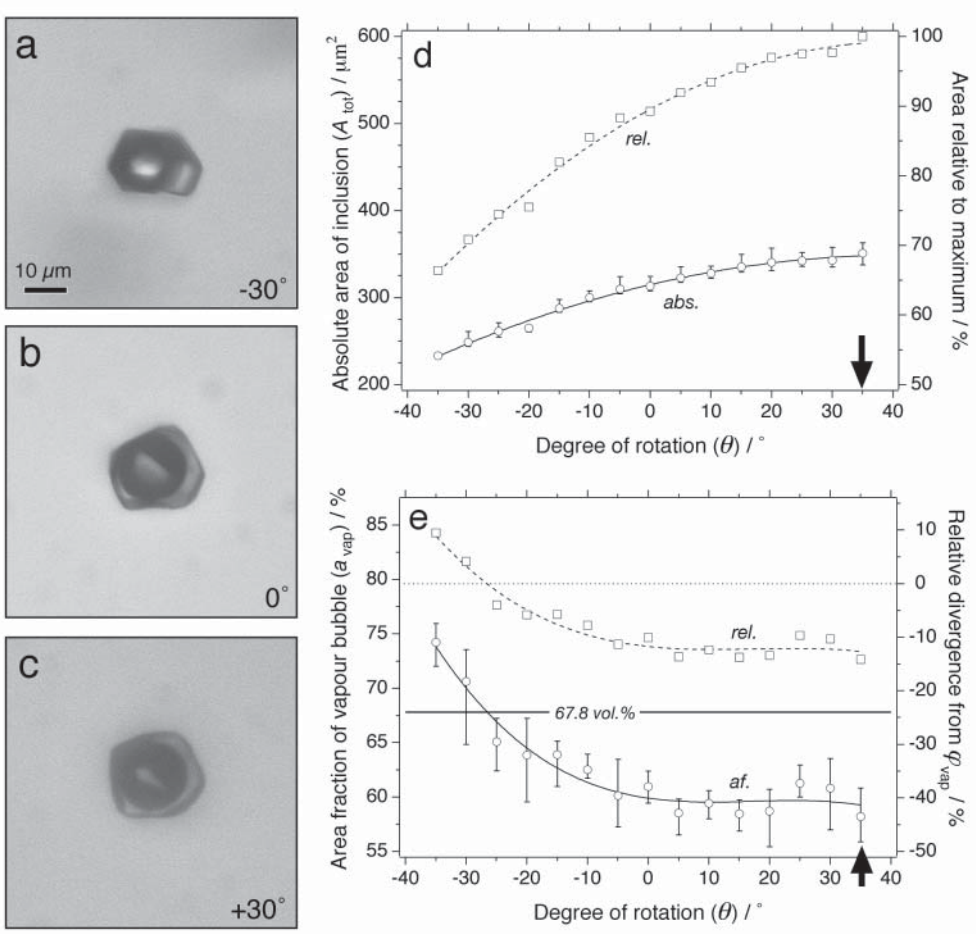

FIGURE 11. Projected areas of a synthetic H_2O inclusion in quartz, containing 67.8 vol% vapor. The shape in (**a**) is crystallographically controlled ("negative crystal"). See caption to Figure 9 for description. The mean absolute divergence at the angle of the maximum projected area (a_{vap}* – φ_{vap}) is –7.8 vol% (arrow in **e**).

TABLE 1. Area and shape measurements of individual, synthetic fluid inclusions

Sample	Inclusion	φ_{vap}	a^*_{vap} (area %)			Δ*	Rel. Δ*	$\left(\frac{\text{Perim.}^2}{4\pi A_{tot}}\right)$		Shape class
		(vol%)	Mean	1σ	1.5σ	(%)	(%)		major/minor	
H_2O crit.	Fig.9	67.8	66.34	1.53	2.30	–1.46	–2.15	1.32	2.18	Regular-elongated
	Fig.10	67.8	68.15	2.10	3.15	0.35	0.52	2.10	4.79	Regular-elongated
	e1	67.8	68.60	1.36	2.04	0.80	1.18	2.56	5.66	Regular-elongated
	e5	67.8	70.20	1.97	2.96	2.40	3.54	1.61	2.32	Regular-elongated
	e6	67.8	65.62	1.46	2.19	–2.18	–3.22	1.21	1.67	Regular-equant
	Fig.11	67.8	60.05	2.43	3.65	–7.75	–11.43	1.05	1.09	Regular-Neg.-crystal
	Fig.12	67.8	54.64	0.73	1.10	–13.16	–19.41	4.12	3.66	Irregular-elongated
	e2	67.8	57.53	2.05	3.08	–10.27	–15.15	4.45	4.37	Irregular-elongated
	e3	67.8	57.43	2.61	3.92	–10.37	–15.29	2.84	1.48	Irregular-equant
	e4	67.8	64.89	3.40	5.10	–2.91	–4.29	2.11	1.88	Irregular-equant
H_2O	Fig.13	17.4	18.57	0.88	1.32	1.17	6.72	1.07	1.33	Regular-equant
	Fig.14	17.4	16.78	0.72	1.08	–0.62	–3.56	3.56	7.79	Regular-elongated
	Fig.15	17.4	12.17	0.23	0.35	–5.23	–30.06	3.18	4.00	Irregular-elongated
H_2O-CO_2	Fig.16	53.8	54.24	2.16	3.24	0.44	0.82	1.07	1.09	Regular-equant
	Fig.17	53.8	54.08	1.82	2.73	0.28	0.52	1.15	1.42	Regular-equant
	Fig.18	53.8	47.49	1.07	1.61	–6.31	–11.73	3.56	4.31	Irregular-elongated

Notes: φ_{vap} = volume fraction of vapor in liquid + vapour inclusion; a^*_{vap} = area fraction of vapour at the rotation angle of maximum projected inclusion area; σ = standard deviation of mean; Δ* = divergence = mean $a^*_{vap} - \varphi_{vap}$; Rel. Δ* = relative divergence = (mean $a^*_{vap} - \varphi_{vap}$)/ φ_{vap}.

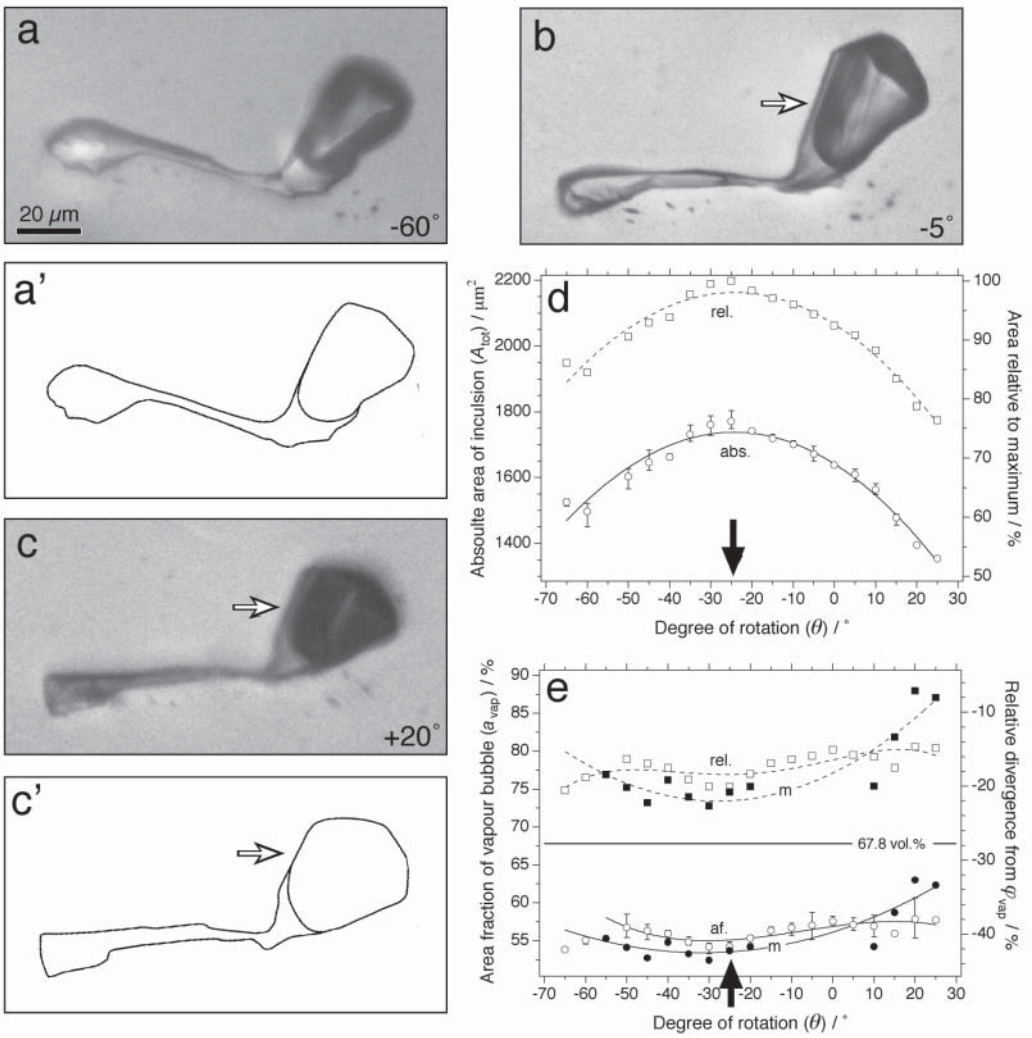

FIGURE 12. Projected areas of an irregular shaped synthetic H_2O inclusion in quartz, containing 67.8 vol% vapor. See caption to Figure 9 for description. (**a**) Inclusion at –60° rotation, photographed in one fixed plane of focus. (a') Scale drawing of the projected inclusion at –60° rotation, for which the focus of the microscope was optimized at each point on the inclusion perimeter. A similar scale drawing is illustrated for the +20° rotation (c and c'). (**e**) Filled symbols represent area fractions measured on scale drawings such as (a') and (c'). Open symbols show area fractions measured on photographs such as (**a**) and (**c**). The mean absolute divergence at the angle of the maximum projected area (a_{vap}* – φ_{vap}) is –13.6 vol% (solid arrow in **e**).

on the relative scale. However, the scatter in the measurements is large, and therefore φ_{vap} is best described as lying within 0.86σ of the five triplicate a_{vap} data near θ* (see also Table 1).

An irregular, slipper-shaped inclusion is shown in Figure 15. Similarly to Figure 12, the complexity of the shape does not allow the entire inclusion to be focused. The dashed A_{tot}-θ curve in Figure 15d falls to 74% of its maximum upon 45° of rotation, approaching the behavior of a flat inclusion (Fig. 8a), but the inclusion defies comparison with any of the geometrical shapes modeled in Figures 4 to 7. All the values of a_{vap} markedly underestimate φ_{vap} (Figure 15e). In this case the reproducibility of the a_{vap} measurements is very good. There is no doubt that at θ* (0°), a_{vap}* underestimates φ_{vap} by 30% on the relative scale. This gross underestimation is comparable to that of the irregular-shaped inclusion in Figure 12.

Measurements of individual synthetic CO_2-H_2O inclusions with 53.8% "vapor"

Figure 16 shows a highly equant inclusion. The dashed A_{tot}-θ curve in Figure 16d falls to only around 80% of its maximum upon 45° of rotation, which in comparable to a cylinder with aspect ratio of 0.4, as shown in Figure 8a. Also the qualitative behavior of the a_{vap}-θ curves in Figure 16e is similar to the hypothetical cylinder modeled in Figure 4; at high angles of rotation, a_{vap} overestimates φ_{vap} by up to 14% on the relative scale. However, at θ* (10°) the mean value of a_{vap}* matches φ_{vap} perfectly.

Figure 17 presents results for an essentially equant inclusion that is slightly elongated and flattened compared to the inclusion in Figure 16. The long axis of the inclusion is oriented at about 30° to the rotation axis of the spindle stage. Similarly to Figure

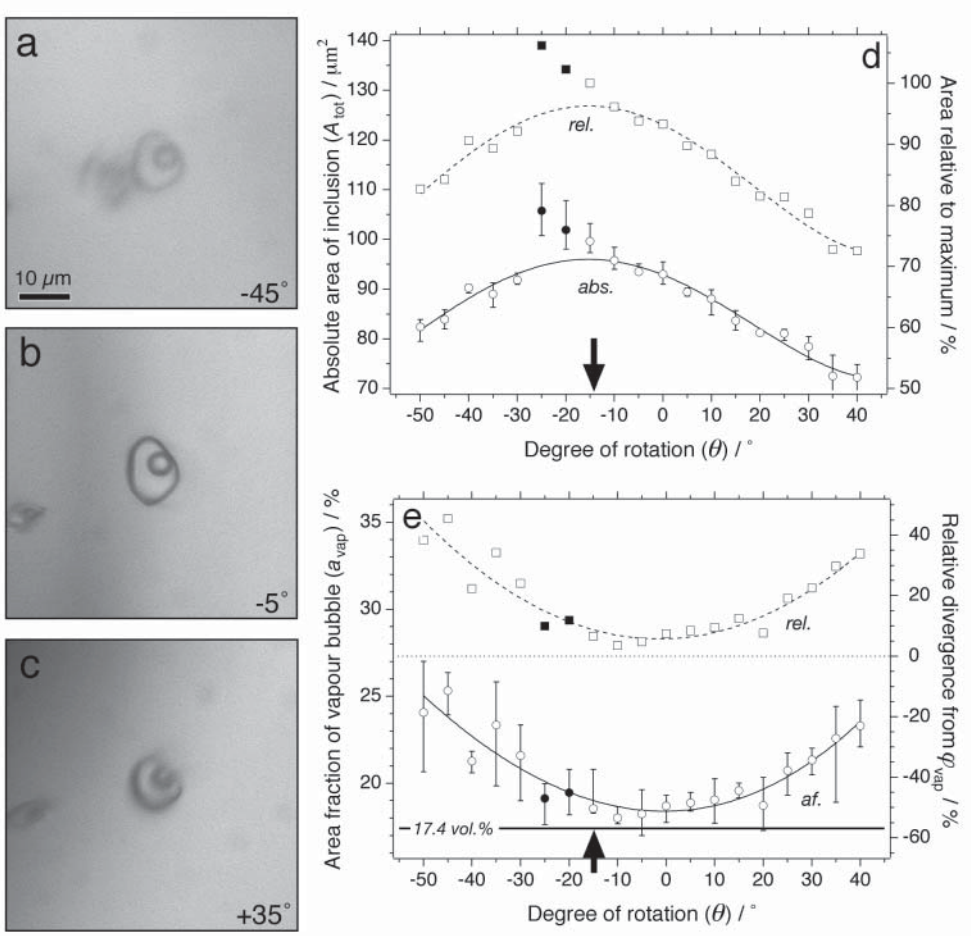

FIGURE 13. Projected areas of an equant, synthetic H_2O inclusion in quartz, containing 17.4 ± 0.07 vol% vapor. See caption to Figure 9 for description. Filled symbols represent measurements where double refraction created strong optical artifacts. These data were ignored during curve-fitting. The mean absolute divergence at the angle of the maximum projected area (a_{vap}* – φ_{vap}) is 1.2 vol% (arrow in **e**).

13, strong double-refraction produces a blurred duplicate image in Figure 17a, hindering accurate measurement at higher angles of rotation. The form of the A_{tot}-θ curves (Fig. 17d) is similar to that in Figure 16. The difference in shape is reflected by the a_{vap}-θ curves (Fig. 17e), which are concave-down and which cut across the φ_{vap} line (cf. Fig. 16e). Nevertheless, the mean a_{vap}* (at θ* = 3°) is still a good estimate of φ_{vap}, exceeding the true value by only 3% on the relative scale.

Figure 18 summarizes measurements from one of the rarer irregular-shaped CO_2-H_2O inclusions. This inclusion displays only minor changes in projected area upon rotation between –20° and +30° (e.g., Figs. 18a and b), demonstrating that it actually has the shape of a club in three dimensions. The vapor bubble resides in the most equant portion of the inclusion (the head of the club). This broadly resembles the calculated geometrical models in which the bubble occupies the widest portion of elongate inclusions, such as curve ***b*** in Figure 6 (cone morphology) and curve ***c*** in Figure 7 (hexagonal prism). In contrast to the equant inclusions in this sample (Figs. 16 and 17), the a_{vap}-θ curves lie far below φ_{vap}. At θ* (13°), the mean a_{vap}* underestimates φ_{vap} by –12% on the relative scale. This large negative divergence is strikingly similar to that found in the two other inclusions with highly irregular shapes: the "ladle" (Fig. 12) and the "slipper" (Fig. 15).

Measurements of assemblages of synthetic inclusions without rotation

Figures 19, 20, and 21 show the projected areas (A_{tot}) vs. a_{vap} of large numbers of inclusions in the three synthetic samples. The measurements were made with the quartz disks in fixed horizontal positions (no rotation). Because all the inclusions in each sample were synthesized at the same experimental conditions, they all have essentially the same φ_{vap} at room temperature, regardless of the variation in their shapes and sizes.

Figure 19 (H_2O inclusions with φ_{vap} = 67.8%) reveals a range of a_{vap} values between 56% and 77%, the scatter being independent of the apparent size (projected area) of the inclusions. The majority of the inclusions have a_{vap} values lower than φ_{vap}, but the mean of the data is 64.1%, which is quite close to φ_{vap}. In Figure 20 (CO_2-H_2O inclusions with φ_{vap} = 53.8 ± 0.25%) the smaller

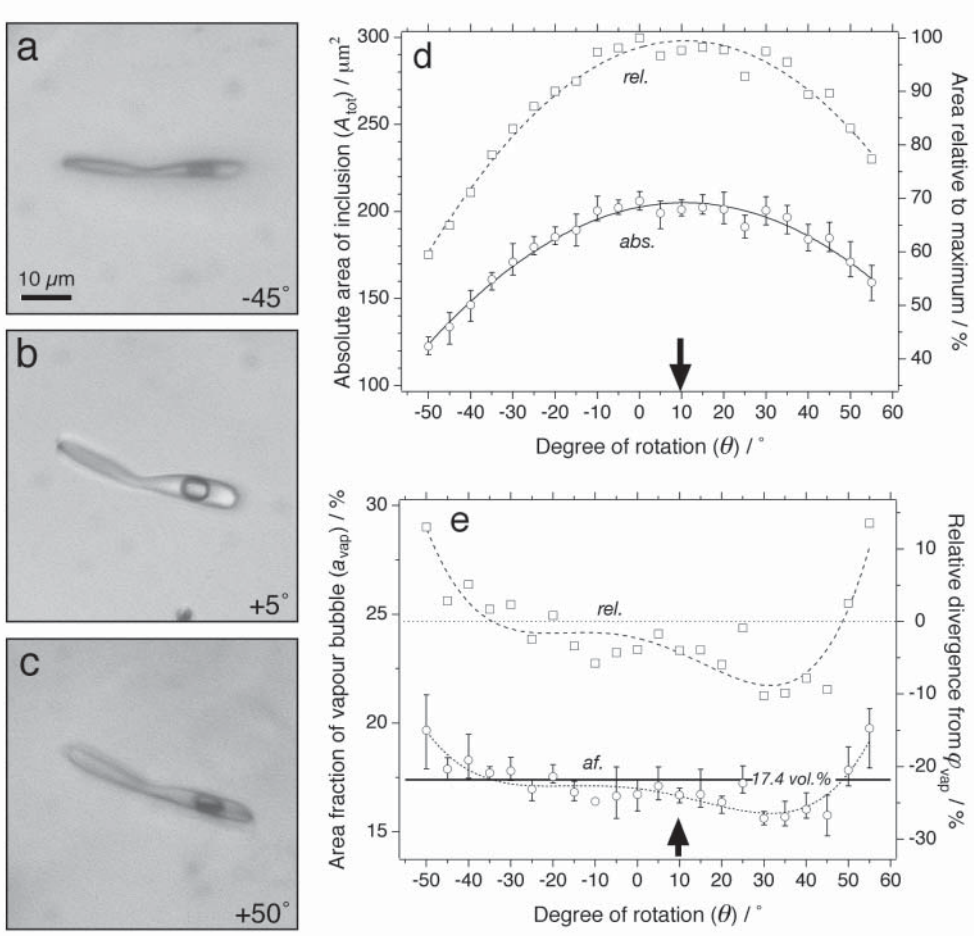

FIGURE 14. Projected areas of an elongate, synthetic H_2O inclusion in quartz, containing 17.4 ± 0.07 vol% vapor. See caption to Figure 9 for description. The mean absolute divergence at the angle of the maximum projected area (a_{vap}* – φ_{vap}) is –0.6 vol% (arrow in **e**).

inclusions show a wide range of a_{vap} (between 45% and 64%) but the range is centered on φ_{vap}. The spread in a_{vap} decreases progressively as the size of the inclusions increases. The largest inclusions display a_{vap} values that only slightly underestimate φ_{vap}. It is noteworthy that the mean of all the 99 a_{vap} data is 53%, which again is very close to φ_{vap}.

The inclusions plotted in Figures 19 and 20 were chosen for measurement indiscriminately, without regard to shape or to the petrographically distinguishable assemblages in the samples. In contrast, the 89 inclusion measurements reported in Figure 21 (H_2O inclusions with φ_{vap} = 17.4 ± 0.07%) are sorted according to assemblages: three healed fractures (each of which has a slightly different orientation within the sample), and a swarm of inclusions along the rim overgrowth of the quartz disk. The healed-fracture assemblages contain more or less regular inclusions, in which a_{vap} (varying between 16 and 25.9 vol%) tends to overestimate φ_{vap} (cf. Figs. 9, 10, 13, and 16). The rim assemblage contains regular and irregular inclusions, many of which are much larger than inclusions in the healed fractures. The a_{vap} values partly overestimate φ_{vap} (regular inclusions) and partly underestimate φ_{vap} (irregular inclusions), with a mean at 17.6%, which yet again is remarkably close to φ_{vap}.

Overall, these samples demonstrate that the mean a_{vap} of assemblages consisting of small numbers of inclusions may significantly overestimate φ_{vap}. It may be presumed, judging from the wide ranges of a_{vap} values observed, that the mean a_{vap} in other samples could just as easily underestimate φ_{vap}. However, the mean a_{vap} values of very large numbers of cogenetic, homogeneously trapped inclusions yield good estimates of φ_{vap} (within ±4% on a relative scale).

Definition and classification of fluid inclusion shapes

The above results on individual inclusions show that rotation of inclusions to the position where their largest areas are projected largely accounts for the dependency of a_{vap} on inclusion orientation. The functional relationship we are searching for (Eq. 7) is thus reduced by one variable:

$$a_{vap} = f(\text{shape}, \varphi_{vap}) \quad (9)$$

The results also show a clear difference in behavior between regularly shaped and irregularly shaped inclusions and between elongate and equant inclusions. To quantify this dependency, an objective classification of two-dimensional shapes is required, including reproducible boundaries between what we qualitatively term "regular," "irregular," "elongate," and "equant."

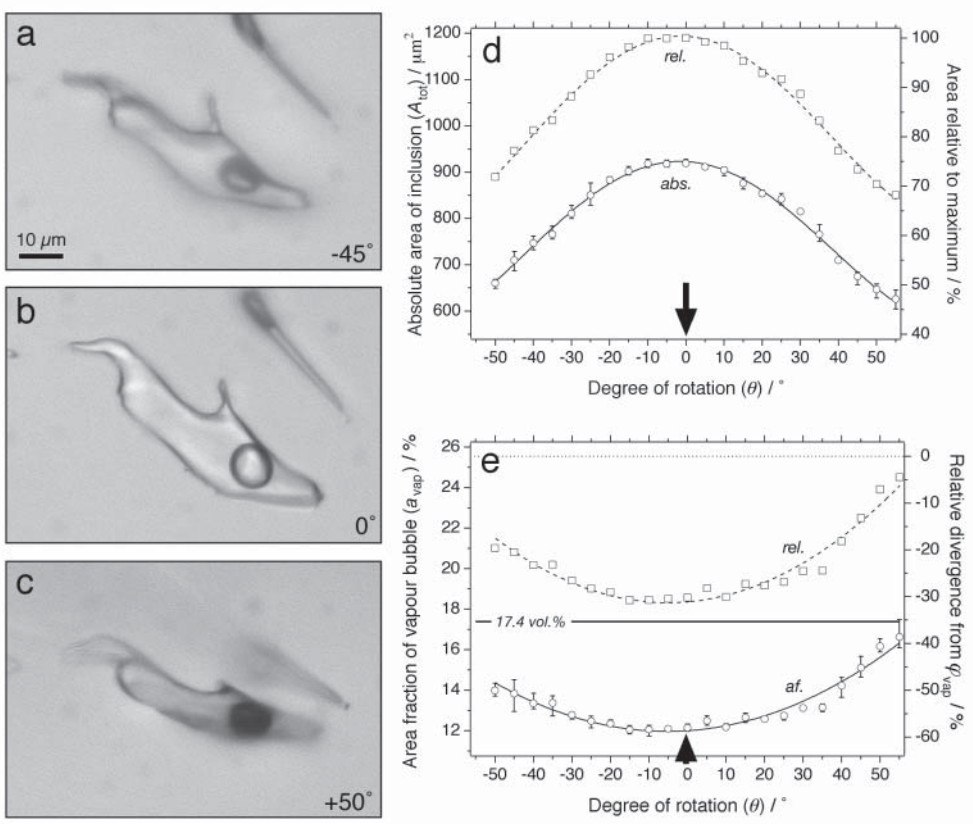

FIGURE 15. Projected areas of an irregularly shaped, synthetic H_2O inclusion in quartz, containing 17.4 ± 0.07 vol% vapor. See caption to Figure 9 for description. The mean absolute divergence at the angle of the maximum projected area (a_{vap}* – φ_{vap}) is –5.2 vol% (arrow in **e**).

Inclusion shapes that are controlled by the crystallography of the host mineral (so-called "negative-crystals" in the fluid inclusion literature) are quite amenable to quantification. Often crystal faces can be indexed and the relative dimensions of the inclusions can be measured. For non-geometrical inclusion shapes, however, there is no precise nomenclature. Terms such as round, spiked, tabular, tubular, etc., are suitable for many problems addressed in the literature, but for present purposes they are too qualitative and too subjective. Given the lack of an appropriate scheme, we propose in the following a quantitative, objective classification of fluid inclusion shapes in two-dimensional projection. The classification is very simple, the aim being to describe the coarse features of shapes in terms of two parameters, rather than to discriminate the huge variety of detailed shapes found in natural inclusions.

The shapes of projected inclusions have several measurable properties that can be quantified numerically with digital image-processing software (e.g., NIH Image version 1.63, ImageJ). The perimeter and the area of a given shape provide a first-order means of differentiating it from other shapes. For example, a circle of any size has a perimeter of $2\pi r$ and an area of πr^2, where r is the radius. Consequently, the ratio of the square of the perimeter and the area multiplied by 4π is always equal to 1 (Fig. 22). The same ratio applied to a square of any size always gives the number 1.2732 (Fig. 22). Increasingly more "irregular" shapes are characterized by increasingly higher values of this ratio. The ratio (perimeter)^2/(4π·area) therefore serves as a quantitative measure of "irregularity" and it is used as an axis parameter in Figure 22. We have arbitrarily set the boundary between what we define as "regular" and "irregular" at a ratio of 1.75.

NIH Image and ImageJ have the capacity to fit an ellipse to any two-dimensional shape. The ratio of the lengths of the major and minor axes of this best-fit ellipse serves as the second parameter defining the shape of an inclusion (ordinate in Fig. 22). In principle, this ratio quantifies the amount of "elongation" of both regular and irregular inclusions. Within the resulting two-parameter space (Fig. 22), we have set an arbitrary boundary at a major/minor ratio of 2 to distinguish between "equant" and "elongate" shapes. Similarly, we have chosen the line that traces the elongation of a four-pronged star (star^4) as the arbitrary boundary between "regular" and "irregular" shapes, as defined by the following equation:

$$y = (x - 1.76)^{0.3} - 2.2618 + 1.5 \cdot x + 1.1 \cdot \ln(x) \quad (10)$$

where x is the ratio (perimeter)^2/(4π·area), and y is the ratio (major axis length)/(minor axis length). Applying both chosen boundaries to Figure 22 divides the field of possible shapes into four regions, or classes: (1) equant and regular, (2) equant and irregular, (3) elongate and regular, and (4) elongate and irregular.

The geometrical models presented in Figures 4 (cylinder), 6 (truncated cone), and 7 ("negative quartz-crystal") are plotted

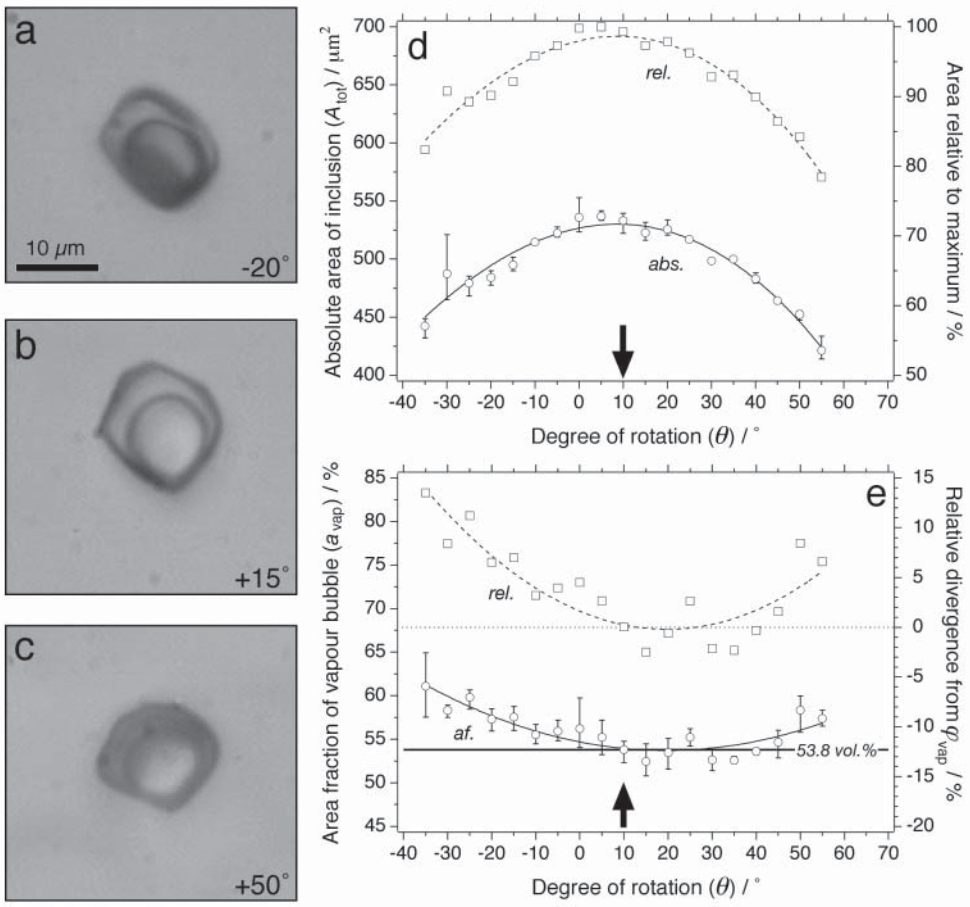

FIGURE 16. Projected areas of an equant, synthetic CO_2-H_2O inclusion in quartz, containing 53.8 ± 0.25 vol% vapor. See caption to Figure 9 for description. The mean absolute divergence at the angle of the maximum projected area (a_{vap}* – φ_{vap}) is 0.4 vol% (arrow in **e**).

in Figure 22 and labeled by the encircled symbols fi4, fi6, and fi7, respectively. The geometrical model in Figure 5 (tetragonal prism) coincides with the dashed curve labeled "rectangles". The thick line segments illustrate how the inclusions change their projected shapes upon rotation. These examples show that one inclusion can span different two-dimensional shape classes, according to the angle at which it is projected. Likewise, inclusions that have identical three-dimensional shapes may be assigned to different shape classes, depending on their orientation within the microscope thick-section. It is also worth noting that, because only two parameters are used to quantify shapes in this scheme, inclusions that look different in detail may actually plot on the same point in Figure 22. The fluid inclusions from Figures 9–18 are plotted in a copy of this diagram (Fig. 23) at their θ* rotation positions. The positions of the additional inclusions listed in Table 1 are also plotted in Figure 23 (labeled e1 to e6). The distribution of points in Figure 23 shows that what we qualitatively perceive as different inclusion shapes (regular vs. irregular, etc.) are nicely discriminated by the two chosen parameters.

DISCUSSION

Table 1 summarizes the essential results of area and shape analyses of the individual, synthetic fluid inclusions presented above. The listed data include the mean of three a_{vap}* determinations for each of the analyzed inclusions, along with the standard deviation (σ) of the five triplicate a_{vap} measurements (i.e., 15 data) nearest to θ*. Values of 1.5σ are also given. The tabulated divergences at θ* (Δ*) are calculated as Δ* = mean a_{vap}* – φ_{vap}. In addition, the "irregularity" and "elongation" parameters are listed with the resulting shape classifications based on Figure 23.

Inspection of the Δ* values in Table 1 reveals a systematic dependency on shape class, which invites generalization: regular inclusions, whether equant or elongate, have small Δ* values, whereas irregular inclusions and the one regular inclusion with a negative-crystal-shape (Fig. 11) have large negative Δ* values. The functional relationship expressed in Equations 7 and 9 is thus reduced to one variable, as originally desired:

$$a_{vap} = f(\varphi_{vap}) \tag{11}$$

In the following we explore the potential of this shape dependency as a means to determine φ_{vap} in natural fluid inclusions, addressing regular, irregular, and negative-crystal shapes in turn. Finally, we discuss the utility of a_{vap} measurements from inclusion assemblages and compare this to the a_{vap}-θ approach for individual inclusions.

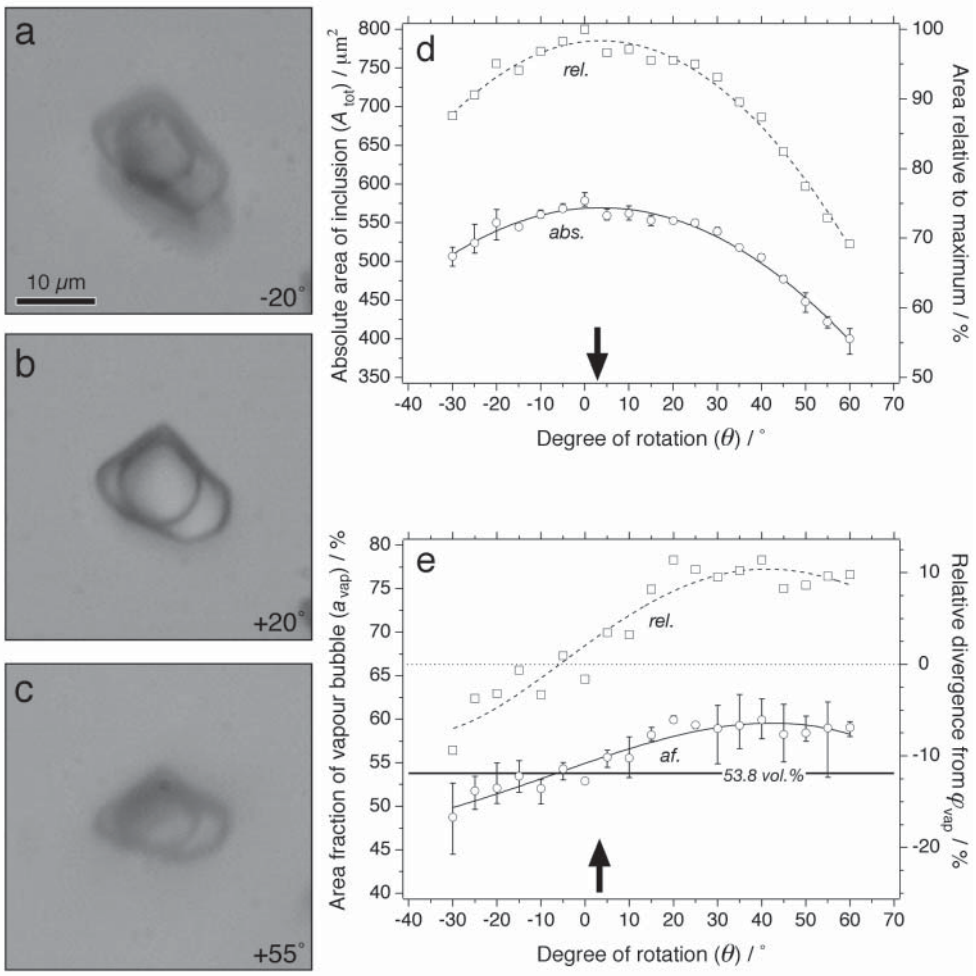

FIGURE 17. Projected areas of a rather flat, equant, synthetic CO_2-H_2O inclusion in quartz, containing 53.8 ± 0.25 vol% vapor. See caption to Figure 9 for description. The mean absolute divergence at the angle of the maximum projected area (a_{vap}* – φ_{vap}) is 0.3 vol% (arrow in **e**).

Regular-shaped inclusions

Table 1 demonstrates that, for all the analyzed "regular" inclusions, whether equant or elongate, the mean a_{vap}* values match the known φ_{vap} values to within 1.5 times the standard deviation of the measurements (i.e., $|\Delta^*| < 1.5\sigma$). The one exception is the inclusion with a negative-crystal shape (Fig. 11). It therefore seems justified, on a purely empirical basis, to propose this relationship as a means to estimate φ_{vap} of natural fluid inclusions that are regular but do not have negative-crystal shapes: thus, φ_{vap} = mean a_{vap}* ±1.5σ. The uncertainty in the determinations (1.5σ) corresponds to ±4% relative to a_{vap}*.

The cause of this consistent relationship between a_{vap}* and φ_{vap} is not completely clear. Regular inclusions have no axes of symmetry, and a less predictable relationship might be expected considering the effects illustrated in Figure 3. One possible explanation is that, by rotating the inclusion to the angle where the maximum surface area is projected, most of the asymmetry in the inclusion is captured by the a_{vap} measurement in the *x*-*y* plane. The minor diameter of the inclusion then lies in the *z*-axis, and in this orientation it seems that the "plus" and "minus" contributions defined in Figure 3 generally cancel each other out.

Nonetheless, it is difficult to imagine that this canceling of competing effects would be exact in all cases. It is probable that there are real differences between the analyzed inclusions, but that these differences fall within the uncertainty of the replicate a_{vap} measurements. Therefore, although replicate measurements of certain favorable natural inclusions (those that are large and situated close to the sample surface) may show smaller scatter than those in Figures 9, 10, 13, 14, 16, and 17, it seems prudent for the time being to apply the global ±4% relative uncertainty found in the present study. More precise a_{vap} measurements may actually imply higher real errors in estimating φ_{vap}.

Irregular-shaped inclusions

In contrast to the "regular" inclusions, Table 1 shows that the mean a_{vap}* values of "irregular" inclusions systematically underestimate φ_{vap}, even taking into account measurement uncertainties. Owing to wetting properties, the liquid phase preferentially fills the narrow arms and tails that give this class of inclusions their mathematical "irregularity," while the vapor bubble sits in the more bulbous regions within the inclusions. It follows that the more irregular the shape, the more the "plus" regions defined

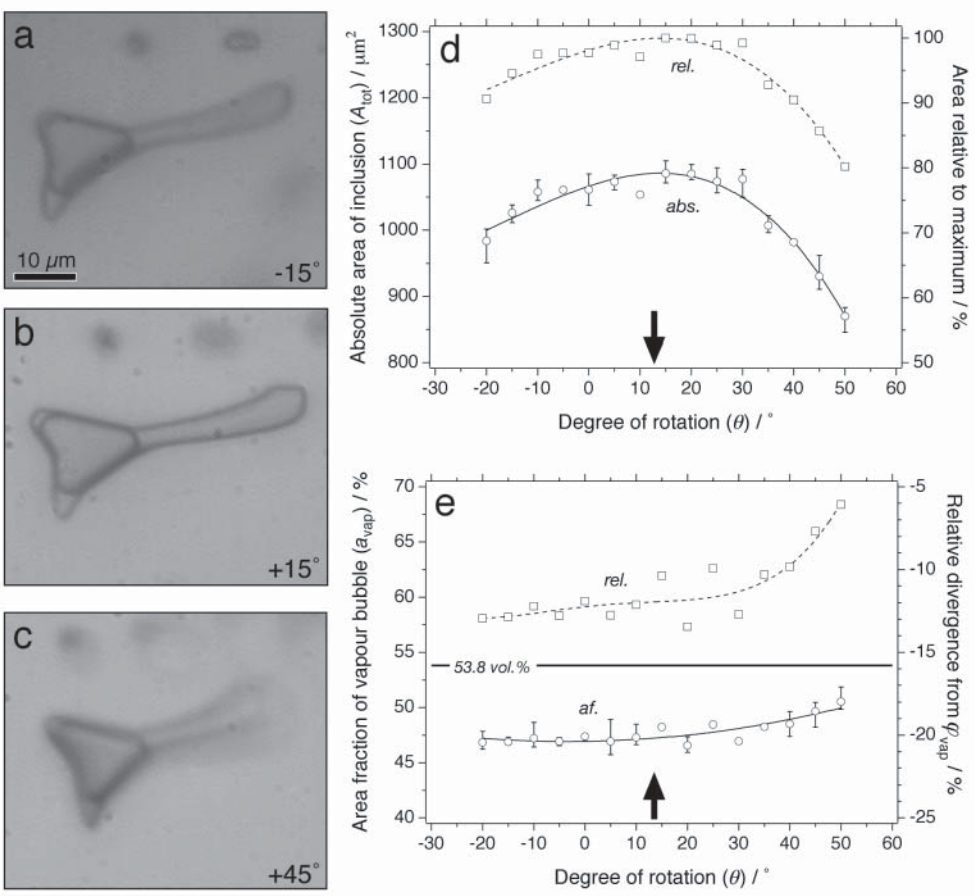

FIGURE 18. Projected areas of an irregularly shaped, synthetic CO_2-H_2O inclusion in quartz, containing 53.8 ± 0.25 vol% vapor. See caption to Figure 9 for description. Dark blebs in the photographs of the inclusions are dust particles on the sample surface, not solid phases within the inclusions. The mean absolute divergence at the angle of the maximum projected area (a_{vap}* – φ_{vap}) is –6.3 vol% (arrow in **e**).

in Figure 3 will dominate a_{vap}. This trend is borne out by the measurements plotted in Figure 23 for irregular inclusions with 67.8 and 53 vol% vapor. The closer the inclusions plot to the regular/irregular boundary, the smaller is the relative divergence between a_{vap}* and φ_{vap}; compare inclusions e4 (rel. $\Delta^* = -4.3\%$) with e3 (–15%) and 18 (–12%) with e2 (–15%) and 12 (–19%). In fact, as indicated in Figure 23, the magnitude of Δ^* appears to follow contours (labeled –10% and –20%) that lie parallel to the regular/irregular boundary. This systematic behavior suggests that the following rule could be applied: $\varphi_{vap} = a_{vap}^* + \Delta^* \pm 1.5\sigma$. On the other hand, the slipper-shaped inclusion (number 15), which contains 17.4 vol% vapor, does not fall on the tentative contours in Figure 23. Although its relative Δ^* is negative, its value is –30%, whereas the contours imply it should be approximately –10%. It seems that the correction contours for irregular inclusions are a function of φ_{vap} itself, not just of inclusion shape. Although more experiments could be conducted to define this function and to fit contours for a range of φ_{vap} values, it is not yet clear how this could be applied objectively to natural inclusions. Accordingly, we propose that the new method to estimate φ_{vap} should be applied only to *regular* inclusions, for which no additional Δ^* correction is necessary.

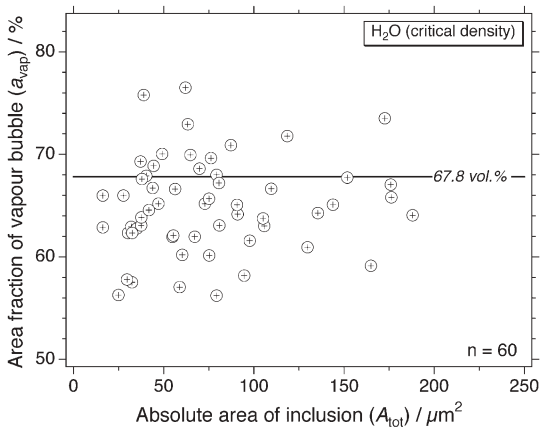

FIGURE 19. Projected area fractions vs. total areas of 60 synthetic H_2O inclusions in quartz, each containing 67.8 vol% vapor (horizontal reference line). The measurements were made with the sample in a fixed orientation (no rotation). The mean area fraction is 64.1%.

Negative-crystal-shaped inclusions

The only measured regular inclusion that does not follow the rule of $\varphi_{vap} = a_{vap}^* \pm 1.5\sigma$ happens to be the only inclusion with

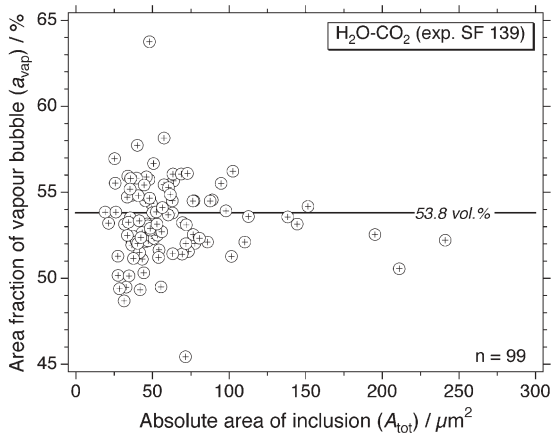

FIGURE 20. Projected area fractions vs. total areas of 100 synthetic CO_2-H_2O inclusions in quartz, each containing 53.8 ± 0.25 vol% vapor (horizontal reference line). Measurements were made with the sample in a fixed orientation (no rotation). The mean area fraction is 53%.

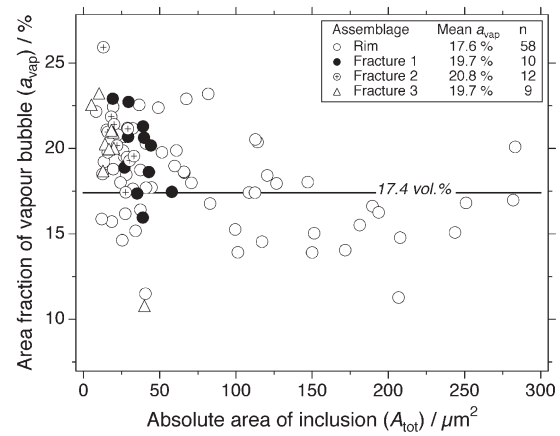

FIGURE 21. Projected area fractions vs. total areas of 89 synthetic H_2O inclusions in quartz, each containing 17.4 ± 0.07 vol% vapor (horizontal reference line). Measurements were made with the sample in a fixed orientation (no rotation). The inclusions are sorted according to petrographic assemblages. The mean area fraction of all 89 inclusions is 17.6%.

a shape that is strongly controlled by the crystallography of the host quartz (i.e., a "negative crystal"; Fig. 11). This result is as expected from the geometrical model in Figure 7, viewed from the angle of largest projected area (curve ***c*** in zones 2 and 3): the "plus" regions in Figure 3 strongly outweigh the "minus" regions when the inclusion is shaped like a negative quartz crystal with $\varphi_{vap} > 25\%$ (note that Fig. 3b itself corresponds to a ***b***-type projection, for which $a_{vap} > \varphi_{vap}$). Unfortunately, the inclusion dimensions modeled in Figure 7 do not mimic inclusion 11 well, and consequently curve ***c*** overestimates the true φ_{vap} by 15% (relative). However, calculation of a new curve ***c*** specifically for the dimensions of inclusion 11 yields $\varphi_{vap} = 68$ to 70% for the measured mean a_{vap}* of 60%, which is acceptably close to the true φ_{vap} value of 67.8%. This example suggests that specific calculations such as those in Figures 5 and 7 could be used to estimate φ_{vap} for natural "regular" inclusions that exhibit crystallographically controlled faces. No universally applicable graphs for this problem are presented here.

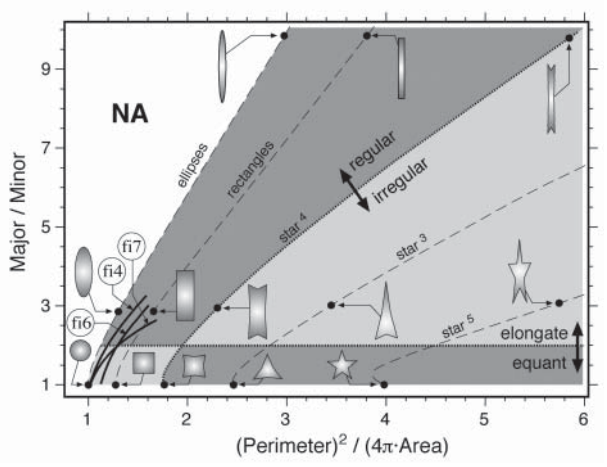

FIGURE 22. Objective shape-classification diagram for two-dimensional projections of fluid inclusions. The abscissa shows the ratio of (perimeter)^2/(4π·area), the ordinate shows the length ratio of major/minor axes of a best-fitting ellipse. Simple geometric shapes are plotted for reference. NA: not accessible. The intersection of the boundaries labeled "regular/irregular" and "equant/elongate" divides the field of accessible shapes into four arbitrary classes (shaded): equant and regular, elongate and regular, equant and irregular, elongate and irregular. Lines fi4, fi6, and fi7 represent the geometrical models illustrated in Figures 4, 6, and 7.

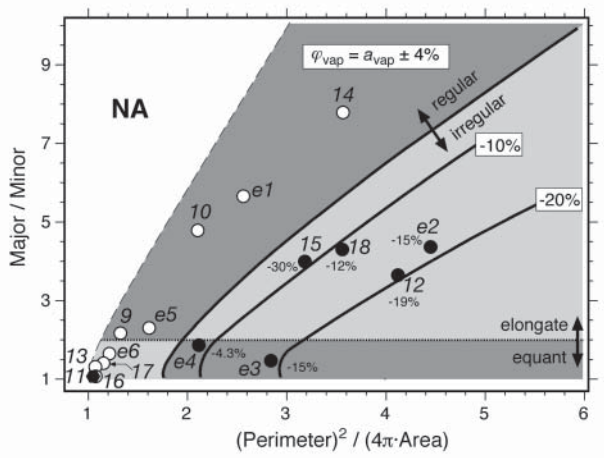

FIGURE 23. Objective shape-classification diagram (see Figure 22 for description) showing positions of the synthetic fluid inclusions analyzed in this study. Numbers 9 to 18 correspond to inclusions shown in Figures 9 to 18. Labels e1 to e6 are additional inclusions. Inclusions that plot in the regular classes and which do not have negative-crystal shapes (open circles) follow the rule $\varphi_{vap} = a_{vap}* \pm 4\%$. The one analyzed inclusion with a negative-crystal shape (number 11) is distinguished by a filled hexagon. Inclusions that plot in the irregular classes (filled circles) are labeled with their respective mean relative divergences ($a_{vap}* - \varphi_{vap}$) in vol%. These follow the rule $\varphi_{vap} = a_{vap}* + \Delta \pm 4\%$, where the magnitude of Δ depends on distance from the regular/irregular boundary and on φ_{vap}. See text for further explanation.

Assemblages of fluid inclusions

Figures 19 and 20 show that the mean of a large number of a_{vap} measurements is a reasonable estimate of φ_{vap}. The question arises as to whether the same approach could be applied to natural

fluid inclusions. It is important to realize that the plotted data in Figures 19 and 20 represent several petrographic assemblages lumped together. This is a valid treatment for synthetic fluid inclusions in which all inclusions in all assemblages can be demonstrated to have the same φ_{vap}. In natural samples, however, it cannot be assumed a priori that every assemblage will have the same φ_{vap} value, even if the assemblages belong to the same generation (e.g., Diamond 2003a). Moreover, often only small numbers of inclusions can be assigned unequivocally to a unique assemblage in natural samples. If only small numbers of inclusions are available per assemblage, then, as illustrated by Figure 21, there appears to be no means of knowing whether the mean a_{vap} value actually overestimates or underestimates φ_{vap}, and whether the error is large or small.

The results in Figure 21 can be explained in light of what has been learned above from the a_{vap}-θ plots of individual inclusions. Inclusions within the same assemblage often show similarities in shapes at any given orientation of the sample, and therefore it is likely that their divergences from φ_{vap} are also similar. For example, the majority of the inclusions in the assemblage marked by filled dots in Figure 21 (which are mostly "regular" according to optical examination) are evidently not oriented such that their largest surfaces are projected through the microscope. By rotating the samples and measuring a_{vap} at each angle of rotation, presumably an angle could be found at which many of the inclusions project their largest surfaces, and the mean of the a_{vap} values may then yield a good estimate of φ_{vap}. However, the effort required for these hundreds of measurements vastly exceeds that required to obtain the same answer from *one* inclusion within the assemblage of interest. Therefore, no profit appears to be gained from measuring the a_{vap} values of entire assemblages.

Conclusions

The above discussion leads to a straightforward and largely objective procedure to determine φ_{vap} in individual "regular" inclusions that consist of liquid and vapor phases. Details of the six step procedure are given in Appendix 1, including a method for adjusting the room-temperature estimate of φ_{vap} to obtain values of φ_{vap} at other temperatures. Careful execution of these steps needs about two hours. The only remaining subjective step, in practice, is deciding when a "regular" inclusion is also a "negative crystal," and when it is not. According to our results so far, any inclusion that displays faces with clear crystallographic control, and with sharp (not rounded) interfacial angles, should be treated as a "negative crystal." Although such inclusions plot in the "regular" field in Figure 23, the rule $\varphi_{vap} = a_{vap}^* \pm 4\%$ does not apply to them. Until a generalized approach becomes available for "negative crystals," we suggest that calculations should be done to model φ_{vap} for each individual inclusion under study.

The procedure outlined in Appendix 1 allows φ_{vap} of individual "regular" inclusions to be determined with a relative uncertainty of ±4%. Thus, an inclusion with $\varphi_{vap} = 0.3$, for example, can be determined to within ± 0.018 absolute. At this stage it seems that improved precision in measuring a_{vap} will not improve the overall accuracy of the φ_{vap} estimates, since the method probably does not discriminate small differences in the shape of inclusions parallel to the *z*-axis of the microscope. It should be recalled that the new method takes no account of the "negative lens" (non-orthogonal light diffraction) effects discussed by previous workers. This is not to say that such effects do not occur; instead, it seems that they are incorporated within the overall ±4% relative uncertainty of the method.

Relative accuracies better than ±4% can be obtained if the results of several inclusions are considered simultaneously. For example, Table 1 lists mean a_{vap}^* values for five "regular" inclusions in the H_2O sample with 67.8% vapor. Selecting the lowest upper estimate ($a_{vap}^* + 4\%$) and the highest lower estimate ($a_{vap}^* - 4\%$) of these data constrains the value of φ_{vap} to lie between 67.4% and 68.2%, which corresponds to a relative uncertainty of only ±0.6%. Clearly, in the case of natural samples, this refined approach can only be applied to inclusions that belong to the same homogeneously trapped assemblage. In practice, the additional effort to obtain such high accuracy (e.g., 10 h measurement time to reach ±0.6% vs. 2 h for ±4%) may not be justified by the application of the results. Errors do not propagate dramatically at low absolute values of φ_{vap} (Fig. 1) and most available equations of state for gas-bearing aqueous fluids, which are used to calculate isochores, have significantly higher uncertainties. Nevertheless, the new method permits highly accurate determinations of φ_{vap} when required.

Application of the φ_{vap} estimates in calculating bulk $V_m - x$ properties of fluid inclusions, e.g., via Equations 3 to 5, is subject to additional uncertainties associated with determining the compositions and molar volumes of the individual liquid and vapor phases. Despite these cumulative uncertainties, the final estimates of bulk $V_m - x$ properties can be very useful in solving geochemical and petrologic problems. Moreover, the new method allows the uncertainties in volume fractions to be quantified and propagated through subsequent calculations, which is a significant advance over earlier approaches.

Acknowledgments

We thank A. Berger for discussions, M. Painsi for helping to test the method, and A. Liechti for assistance in the hydrothermal laboratory at the University of Bern. A. van den Kerkhof and J. Pironon kindly provided constructive reviews of the manuscript. This study was supported by Swiss National Science Foundation grant 200021–103905 to L. W. Diamond.

References cited

Andersen, T., Frezzotti, M.-L., and Burke, E.A.J. (2001) Fluid inclusions: Phase relationships - methods - applications. Lithos, 55, 1–320.

Anderson, A.J. and Bodnar, R.J. (1993) An adaptation of the spindle stage for geometric analysis of fluid inclusions. American Mineralogist, 78, 657–664.

Aplin, A.C, Macleod, G., Larter, S.R., Pedersen, K.S., Sorensen, H., and Booth, T. (1999) Combined use of confocal laser scanning microscopy and PVT simulation for estimating the composition and physical properties of petroleum in fluid inclusions. Marine and Petroleum Geology, 16, 97–110.

Bakker, R.J. (2003) Package FLUIDS 1. Computer programs for analysis of fluid inclusion data and for modeling bulk fluid properties. Chemical Geology, 194, 3–23.

Bakker, R.J. and Diamond, L.W. (2000) Determination of the composition and molar volume of H_2O-CO_2 fluid inclusions by microthermometry. Geochimica et Cosmochimica Acta, 64, 1753–1764.

Bodnar, R.J. and Sterner, S.M. (1987) Synthetic fluid inclusions. In G.C. Ulmer and H.L. Barnes, Eds., Hydrothermal Experimental Techniques, pp. 423–457. Wiley, New York.

Bodnar, R.J., Reynolds, T.J., and Kuehn, C.A. (1985) Fluid inclusion systematics in epithermal systems. In B.R. Berger and P.M. Bethke, Eds., Geology and Geochemistry of Epithermal Systems. Reviews in Economic Geology, 2, 73–97.

Diamond, L.W. (2003a) Introduction to gas-bearing aqueous fluid inclusions. In I.M. Samson, A.J. Anderson, and D.D. Marshall, Eds., Fluid Inclusions: Analysis and Interpretation, p. 101–158. Mineralogical Association of Canada.

——— (2003b) Systematics of H_2O inclusions. In I.M. Samson, A.J. Anderson, and D.D. Marshall, Eds., Fluid Inclusions: Analysis and Interpretation, p. 55–79.

Mineralogical Association of Canada.
——— (2003c) Glossary: Terms and symbols used in fluid inclusion studies. In I.M. Samson, A.J. Anderson, and D.D. Marshall, Eds. Fluid Inclusions: Analysis and Interpretation, p. 363–372. Mineralogical Association of Canada.
Diamond, L.W. and Akinfiev, N.N. (2003) Solubility of CO_2 in water from –1.5 to 100 °C and from 0.1 to 100 MPa: Evaluation of literature data and thermodynamic modeling. Fluid Phase Equilibria, 208, 263–288.
Pironon, J., Canals, M., Dubessy, J., Walgenwitz, F., and Laplace-Builhe, C. (1998) Volumetric reconstruction of individual oil inclusions by confocal scanning laser microscopy. European Journal of Mineralogy, 10, 1143–1150.
Roedder, E. (1967) Fluid inclusions as samples of ore fluids. In H.L. Barnes, Ed., Geochemistry of Hydrothermal Ore Deposits, 515–574. Rinehard and Winston, New York.
——— (1972) Composition of fluid inclusions. Geological Survey Professional Paper, 440-JJ, United States Government Printing Office, Washington, pp. 164.
——— (1984) Fluid Inclusions, vol. 12. Reviews in Mineralogy, Mineralogical Society of America, Chantilly, Virginia.
Samson, I.M., Anderson, A.J., and Marshall, D.D. (2003) Fluid Inclusions: Analysis and Interpretation. Short Course 32. Mineralogical Association of Canada.
Saylor, C.P. (1965) A study of errors in the measurements of microscopic spheres. Applied Optics, 4, 477–486.
Shepherd, T.J., Rankin, A.H., and Alderton, D.H.M. (1985) A Practical Guide to Fluid Inclusion Studies. Blackie, Glasglow, U.K.
Wagner, W. and Pruss, A. (2002) The IAPWS formulation 1995 for the thermodynamic properties of ordinary water substance for general and scientific use. Journal of Physical and Chemical Reference Data, 31, 387–535.

MANUSCRIPT RECEIVED NOVEMBER 4, 2004
MANUSCRIPT ACCEPTED MAY 2, 2005
MANUSCRIPT HANDLED BY ALAN ANDERSON

APPENDIX 1: RECOMMENDED PROCEDURE TO MEASURE THE VOLUME FRACTION OF PHASES IN INDIVIDUAL INCLUSIONS CONSISTING OF LIQUID AND VAPOR

Five steps are given below to determine the value of φ_{vap} at room temperature. A sixth step explains how to adjust this value to estimate φ_{vap} at other temperatures. It is assumed that the reader has studied the main body of this article.

Selection of target inclusions for measurement

Qualitative optical estimates of a_{vap} should be used, according to traditional practice, to distinguish homogeneous from heterogeneous entrapment of individual petrographic assemblages. For homogeneously trapped inclusions, quantitative φ_{vap} determinations from only one to three inclusions per assemblage are sufficient, in principle, to define φ_{vap}. For heterogeneously trapped inclusions, more measurements may have to be made per assemblage to find the extreme values of φ_{vap} in the liquid-rich and gas-rich end-members (e.g., Diamond 2003b). For both homogeneously and heterogeneously trapped assemblages, optimal inclusions for measurement are (1) large (the errors in measuring a_{vap} are minimized), (2) regular in shape (irregular inclusions cannot be quantified with the current methodology), and (3) situated near the surface of the sample (the clarity of inclusions upon rotation is maximized).

Rotation of inclusion samples

Mount the sample on the spindle stage and center the axis of rotation on the target inclusion. Using the highest microscope magnification possible (usually a 36× or a 40× long working-distance objective lens), take digital photographs of the inclusion at 5° intervals of rotation (+ and –), over as large a range of angles as permitted by the clarity of the images. Record the orientation of the spindle-stage axis and the length scale (in μm) of the photographs (for routine analysis, pixels are sufficient). For each photograph, record the angle of rotation. Use a polarizer below the sample to reduce double refraction at high angles of rotation. For inclusions that are not entirely focused at a given position, photographs are unsuitable for area measurements. Better accuracy is obtained by making a drawing of the inclusion while optimizing the focus at each point along the perimeters of the inclusion and the vapor bubble. Drawings can be made using a projection tube mounted on the microscope or by tracing on a clear plastic sheet placed over the inclusion image displayed on a computer screen.

Measurement of A_{tot} and a_{vap}

Import the digital photographs or scanned drawings into *ImageJ* (freeware obtainable at http://rsb.info.nih.gov/). Use the Polygon Selections tool to measure the length scale of the photograph in pixels. Then within the *Analyze* menu, select the *Set Scale* option and enter this pixel length to define the scale of the photographs (typically around 6 pixel/μm for a 40× objective lens). In the *Set Measurement* option, select the parameters for measurement (*Area*, *Perimeter*, *Fit Ellipse*) and specify their precision to three decimal places. For each image, use the *Polygon Selection* tool to draw around the perimeter of the inclusion, then from the *Analyze* menu execute *Measure* to record the values of the parameters. Repeat the measurements for the vapor bubble. Care must be taken to trace around the *outside* edges of the dark shadows that define the inclusion and bubble perimeters; these correspond most closely to the true projection of the inclusion. To enhance accuracy, the measurements should be repeated at least thrice; we recommend tracing once clockwise then once anticlockwise, then the image should be enlarged to 200% and traced again. Calculate the area fraction of the vapor (a_{vap}) for each image.

Initial Estimate of a_{vap}

Plot the inclusion areas, A_{tot}, and the calculated a_{vap} values as a function of rotation angle θ, as shown in Figures 9 to 18. Fit the data sets to polynomial functions by least-squares regression. If the A_{tot}-θ function displays a maximum, locate the corresponding a_{vap} value at this angle. This particular value of a_{vap} is denoted a_{vap}*. For a range of angles near a_{vap}* (e.g., the five nearest sets of triplicate a_{vap} measurements, corresponding to 15 data), calculate the local standard deviation (σ) of a_{vap} with respect to the polynomial fit. This procedure yields the *initial estimate* (a_{vap}* ± σ).

Discrimination of inclusion shapes and estimation of φ_{vap}

Spherical inclusions. If the fitted A_{tot}-θ function is flat, the inclusion is spherical, and so the a_{vap}-θ function should also be essentially constant. In this case, a selection of the five triplicate sets of a_{vap} measurements that were made under the best observation conditions (clarity of inclusion and bubble outlines) can be used to calculate the mean and standard deviation of a_{vap}. The resulting mean a_{vap} ± σ can now be plotted on curve ***s*** in Figure 4 to determine φ_{vap} ± σ.

Flat inclusions. The inclusion can be identified as being flat if (1) the a_{vap}-θ curve is nearly constant and (2) the A_{tot}-θ curve is closely described by the function $A_{tot} = 100 \cdot \cos\theta$ over at least 45° of rotation (i.e., A_{tot} falls to 71% of its maximum

upon 45° of rotation). If these two criteria are fulfilled, then $\varphi_{vap} = a_{vap}^* \pm \sigma$.

"Negative-crystal" inclusions. Examine the photographs to identify whether the inclusion shape is strongly controlled by the crystallography of the host mineral. Such "negative-crystals" have straight facet outlines in projection, and sharp (not rounded) interfacial angles. Inclusion outlines that are only *partly* faceted in this way also qualify for the present purposes as negative crystals (cf. Fig. 11). Calculate the theoretical volume of the inclusion by assuming it to be a perfect geometrical body (e.g., hexagonal prism with pyramids for quartz; cube for fluorite) with outer dimensions as observed in the series of photographs. For elongate negative-crystal shapes, identify the maximum angle between the longest axis of the inclusion and the rotation axis of the spindle stage (α_{max}, see also Fig 8c and d). Taking the geometrical effect of α_{max} into account, calculate theoretical a_{vap}^* values for a range of model φ_{vap} values and plot them in a new a_{vap}^*-φ_{vap} curve, similar to ***c*** in Figure 7. The measured mean $a_{vap}^* \pm \sigma$ can now be plotted on the new curve to obtain $\varphi_{vap} \pm \sigma$ of the inclusion.

Other inclusion shapes (i.e., those that are not spherical, flat, or negative-crystals)

Using the Area, Perimeter, and Fit Ellipse measurements performed in step 4, plot the position of the inclusion on the shape-classification diagram (Fig. 23). For all inclusions that fall in the *regular* field (whether elongate or equant; Eq. 10), check that $1.5\sigma < (a_{vap}^* \pm 4\%)$. If so, the recommended global uncertainty of ±4% (relative to a_{vap}^*) can be applied with confidence; thus $\varphi_{vap} = a_{vap}^* \pm 4\%$. If $1.5\sigma > (a_{vap}^* \pm 4\%)$, which reflects optical conditions worse than those found in the present study, the best estimate to use is $\varphi_{vap} = a_{vap}^* \pm 1.5\sigma$. Inclusions that plot in the *irregular* field cannot be analyzed accurately with the present methodology.

Estimation of φ_{vap} at temperatures above or below room temperature

The current design of the spindle stage (Anderson and Bodnar 1993) does not permit inclusions to be heated or cooled; all measurements must be performed at room temperature. If φ_{vap} is required at another temperature (e.g., to perform calculations of bulk $V_m - x$ properties), then the room-temperature estimate of φ_{vap} obtained using the above method can be roughly adjusted by measuring the change in radius (r) of the vapor bubble between room temperature (T_1) and the target temperature (T_2). Thus, for a spherical bubble (assuming that the volume of the total inclusion remains constant):

$$\varphi_{vap}(T_2) = \varphi_{vap}(T_1) \cdot \left(\frac{r_{vap}(T_2)^3}{r_{vap}(T_1)^3} \right) \quad \text{(A1)}$$

For example, if $\varphi_{vap}(20\ °C) = 0.2$ and $r_{vap}(20\ °C) = 4\ \mu m$, and if the radius of the spherical bubble increases to 5 μm upon cooling to –20 °C, then $\varphi_{vap}(-20\ °C) = 0.2 \cdot (5^3 / 4^3) = 0.39$. Similarly, for a flat bubble:

$$\varphi_{vap}(T_2) = \varphi_{vap}(T_1) \cdot \left(\frac{r_{vap}(T_2)^2}{r_{vap}(T_1)^2} \right) \quad \text{(A2)}$$

For deformed bubbles with shapes between spherical and flat, no simple solution is offered other than the upper and lower bounds imposed by Equations 12 and 13.